

# Density Functional Theory for Battery Materials

Qiu He, Bin Yu, Zhaozhai Li, and Yan Zhao\* 

Batteries are the most widely used energy storage devices, and the lithium-ion battery is the most heavily commercialized and most widely used battery type in the industry. However, the current rapid development of society requires a major advancement in battery materials to achieve high capacity, long life cycle, low cost, and reliable safety. Therefore, many new efficient energy storage materials and battery systems are being developed and explored, and their working mechanisms must be clearly understood before industrial application. In recent years, density functional theory (DFT) has been employed in the energy storage field and has made significant contributions to the understanding of electrochemical reaction mechanisms and to virtual screening of promising energy storage materials. In this review, the applications of DFT to battery materials are summarized and exemplified by some representative and up-to-date studies in the literature. The main focuses in this review include the following: 1) structural stability estimation by cohesive energy, formation energy, Gibbs free energy, and phonon dispersion spectra calculations; 2) the Gibbs free energy calculations for electrochemical reactions, corresponding open-circuit voltage, and theoretical capacity predictions of batteries; 3) the analyses of molecule orbitals, band structures, density of states (DOS), and charge distribution of battery materials; 4) ion transport kinetics in battery materials; 5) simulations of adsorption processes. We conclude the review with the discussion of the assessments and validation of the popular functionals against several benchmarks, and a few suggestions have been given for the selection of density functionals for battery material systems.

## 1. Introduction

Global energy shortage and environmental pollution have raised a red flag for humanity, urging us to change the traditional energy acquisition methods and instead utilize green energy sources such as solar energy,<sup>[1]</sup> wind energy,<sup>[2]</sup> geothermal energy,<sup>[3]</sup> and tidal energy.<sup>[4]</sup> These energies are usually collected in the form of electrical energy and then delivered to users, such that energy storage device plays a pivotal role in determining the energy utilization ratio.<sup>[5,6]</sup> The most commonly used energy storage device is battery, especially the lithium-ion battery (LIB). However, the current energy and power density, safety, and life cycle of commercialized LIBs hardly meet the needs created by recent societal developments.<sup>[7–10]</sup> Furthermore, the production costs of LIBs for large-scale energy storage is expensive at present. Consequently, many researchers are devoted to developing or designing new materials for LIBs, including cheaper electrode materials with high theoretical capacities, safer electrolyte materials, and more efficient separators.<sup>[11]</sup> Meanwhile, new battery systems are being explored, such as sodium, potassium, zinc, aluminum, calcium, and magnesium ion batteries (SIB, PIB, ZIB, AIB, CIB, MIB),<sup>[12–19]</sup> lithium-sulfur batteries (LSB),<sup>[20]</sup> and metal-air batteries.<sup>[21]</sup> Although there have been tremendous efforts, there are

many technical hurdles for the commercialization of these new battery systems. One challenging obstacle is that the reaction mechanisms of new battery systems at the atomic/molecular levels are difficult to investigate experimentally, even though the characterization techniques have been developed rapidly. However, a better understanding of the working mechanisms of battery materials is crucial for developing new advanced battery materials toward industrial applications.

Based on the Born–Oppenheimer approximation of the Schrodinger equation, the ground-state electronic structure and nuclear repulsion in a solid material determine its lattice constants, cohesive energies, band structures, surface reactivity, thermochemistry, rate constants, and other physical and chemical properties. The Kohn–Sham density functional theory (DFT) has become the most predominant tool in computational materials science and solid-state physics for a numerical solution to the Schrodinger equation.<sup>[22,23]</sup> The accuracy of a DFT calculation depends upon the quality of the exchange-correlation (XC) functional. The past three decades have seen remarkable progress in the development and application of XC density functionals. In the first generation of functionals, called local spin density approximation (LSDA), the density functionals depend only on the local spin densities. Although LSDA

Q. He, B. Yu

State Key Laboratory of Silicate Materials for Architectures, International School of Materials Science and Engineering, Wuhan University of Technology, Hubei 430070, China

Z. Li

State Key Laboratory of Advanced Technology for Materials Synthesis and Processing, Wuhan University of Technology, Hubei 430070, China  
Prof. Dr. Y. Zhao

State Key Laboratory of Silicate Materials for Architectures, International School of Materials Science and Engineering, Wuhan University of Technology, Hubei 430070, China

E-mail: yan2000@whut.edu.cn

Prof. Dr. Y. Zhao

The Institute of Technological Sciences, Wuhan University, Hubei 430072, China

E-mail: yan2000@whut.edu.cn

 The ORCID identification number(s) for the author(s) of this article can be found under <https://doi.org/10.1002/eem2.12056>.

DOI: 10.1002/eem2.12056

performs surprisingly well for the prediction of lattice constants, it is not a useful computational tool for chemistry because LSDA severely underestimates barrier height for chemical reactions and overbinds the chemical bonds. A step forward is the generalized gradient approximation (GGA), and this family of functionals depends on the spin density and its gradient. GGA functionals have been shown to be much more useful than LSDA functionals for chemical bond energies, but they still underestimate band gaps, barrier heights, and noncovalent interactions. The third-generation functionals (meta-GGAs) employ spin kinetic energy densities and/or the spin density Laplacian. LSDAs, GGAs, and meta-GGAs are local or semilocal functionals, and they can be mixed with nonlocal Hartree–Fock (HF) exchange as justified by the adiabatic connection theory. Functionals containing HF exchange are usually called hybrid functionals and are often more accurate than local functionals for band gap predictions, but the application of HF exchange in solid-state physics is less common because of the much higher computational cost.

In recent decades, DFT has been increasingly employed to simulate the structures and elucidate the activities of energy storage materials, and the predominant functionals applied in battery materials science are the GGA functionals, especially the Perdew–Burke–Ernzerhof (PBE) GGA. DFT is adopted to calculate the thermodynamic properties, electronic structures, reaction kinetics, and ion transport paths of electrodes/electrolytes for batteries.<sup>[24–28]</sup> As compared to experiments, DFT calculations show advantages for exploring reaction mechanisms at the atomic level and for virtual screening new battery materials to reduce the development cost. In the literature of this research area, majority of the studies focus on experiments, with DFT as an auxiliary for verification.<sup>[29–36]</sup> Some studies use DFT for comprehensive theoretical analysis of battery materials without experiments,<sup>[37–46]</sup> while some studies place equal emphasis on experiments and DFT calculations.

In this review, we introduce some recent applications of DFT in battery materials science, and the paper is organized as follows: Section 2 discusses the structural stability estimation of a battery material with DFT calculations. In particular, the cohesive energy, formation energy, Gibbs free energy, and the phonon dispersion spectrum are discussed in detail for this type of applications. Section 3 describes the estimation of open-circuit voltage (OCV) and theoretical capacity of a battery based on the Gibbs free energy calculations. Section 4 presents the electronic structure analysis of battery materials, including HOMO/LUMO gaps, band structures, density of states (DOS), and charge distributions. Section 5 discusses the ion transport kinetics in battery materials, which is related to the ionic transport rates that affect the rate capacity of batteries. Section 6 describes the adsorption process simulation of ions or molecules, which is widely used to investigate the ion storage capability and the electrochemical reaction mechanism. Section 7 presents the assessments and validations of the popular density functionals for the battery material systems, and provides some recommendations and warnings for choosing density functionals for the study of battery materials. Section 8 concludes the paper.

## 2. Structural Stability Estimation

The structural stability of a battery material is a dominant factor for its cycling lifetime, and the stability of a battery material can be estimated from the calculations of cohesive energy, formation energy, Gibbs free energy, and the phonon dispersion spectrum. In this section, these four methods are introduced, and several representative electrode materials are given to show the applications of DFT in battery materials science.



**Qiu He** is a Ph.D. student under the supervision of Prof. Yan Zhao at Wuhan University of Technology where she majors in transition metal oxide electrode materials of lithium-ion battery/lithium-sulfur battery and the application of density functional theory in battery-related materials.



**Bin Yu** is a M.S. student under the supervision of Prof. Yan Zhao at Wuhan University of Technology. His research focuses on the synthesis of metal organic frameworks and their application in batteries, and also the computational material sciences in batteries.



**Zhaohuai Li** is a Ph.D. student under the supervision of Prof. Liqiang Mai at Wuhan University of Technology. He ever-studied silicon-based anode of lithium-ion battery. Currently, his research mainly focuses on lithium-sulfur battery, including sulfur cathode host materials, separator materials, and metallic lithium anode materials.



**Yan Zhao** obtained the Ph.D. of engineering at Sichuan University in 1999 and Ph.D. of Chemistry at University of Minnesota in 2005. Now, he is a chief professor at Wuhan University of Technology and leads a research group that combines experiments and theoretical modeling to development the new-generation energy storage materials.

His research centers on the developments and applications of the new theoretical/computational methods for chemistry and materials science.

### 2.1. Cohesive Energy

Cohesive energy refers to the energy released when isolated free atoms form compounds, and it can be calculated using the following equation:

$$E_{co} = \frac{m \times E(A) + n \times E(B) - E(A_mB_n)}{m + n} \quad (1)$$

In the Equation (1),  $A_mB_n$  is a compound; m and n are the number of A and B in the formula;  $E(A_mB_n)$ ,  $E(A)$ , and  $E(B)$  are the energies of compound  $A_mB_n$ , isolated atom A, and isolated atom B, respectively; and  $E_{co}$  is the cohesive energy. In general, the structure is more stable when its cohesive energy is higher.

Recently, a report of cohesive energy calculations of the covalent organic frameworks (COFs) has been published. COFs are a class of materials with strong covalent bonds, high porosity, and low density, and they are potential anode materials for LIBs. Structural stability is the premise of their practical application in battery. In this context, Fang et al. calculated the cohesive energies for a COF material, NUS-2 ( $[C_9H_6O_3N_3]_n$ , a copolymer of triformylphloroglucinol and hydrazine hydrate), and its complexes with 1, 6, 12, and 14 lithium atoms in a monolayer supercell, respectively.<sup>[47]</sup> The cohesive energies were calculated by Equation (1). Their calculations demonstrate that NUS-2 has a large cohesive energy (5.6 eV/atom), corresponding to its excellent structural stability. They also found that the complex of NUS-2 with 14 lithium atoms still has a relatively high cohesive energy (4.6 eV/atom), which confirms that NUS-2 is a potential LIB materials of high thermodynamic stability and large lithium storage capability.

## 2.2. Formation Energy

Formation energy represents the energy change when a solid or compound is formed from its constituent elements in their standard state. The formation energy of a compound can be calculated from the following equation:

$$E_f = \frac{m \times E(A) + n \times E(B) - E(A_mB_n)}{m + n} \quad (2)$$

Although Equation (2) is similar to Equation (1),  $E(A)$  and  $E(B)$  are the energies of constituent elements in their standard states instead of isolated atoms. The more positive the formation energy, the more stable the structure. It is more practical to predict the stability of a structure through its formation energy than cohesive energy because a compound is rarely synthesized from isolated atoms.

The two-dimensional (2D) materials are preferential as battery materials owing to their high specific capacity, among which Si and Ge were predicted to have high capacity but low stability.<sup>[48–51]</sup> Interestingly, the 2D alloy SiGe can remedy the defects. Recently, Arindam Sanyal et al.<sup>[52]</sup> calculated the formation energy of SiGe with Equation (2), and they obtained the formation energy per unit cell is 1.51 eV, which indicates the good thermodynamic stability of 2D SiGe.

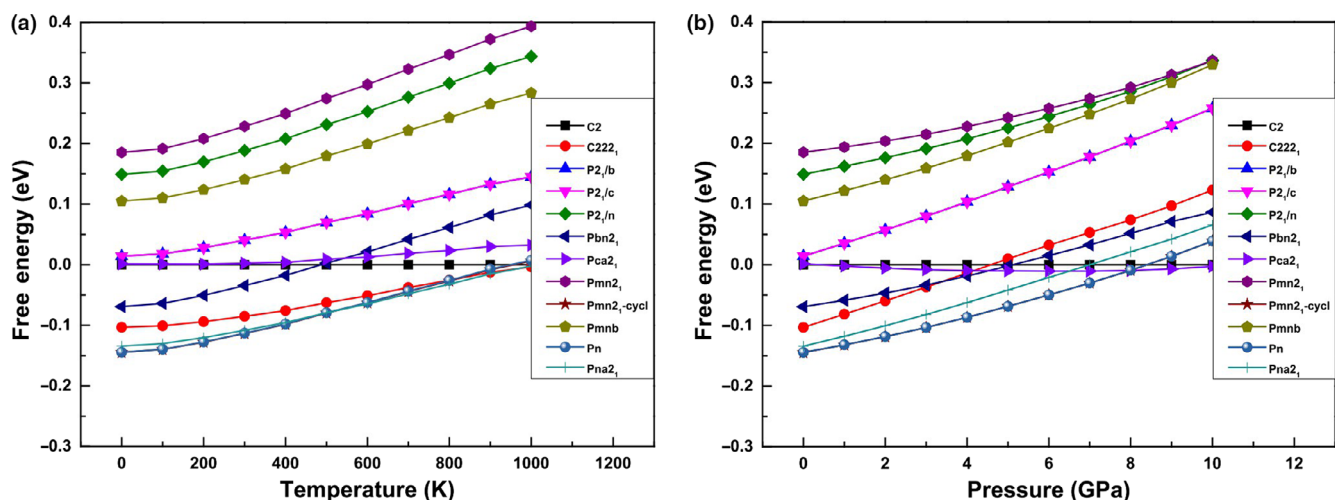


**Figure 1.** a) Temperature-dependent and b) pressure-dependent free energy curves (relative to  $C_2$ ) of different  $Na_2FeSiO_4$  structures. Reprinted with permission.<sup>[53]</sup> Copyright 2018, Elsevier.

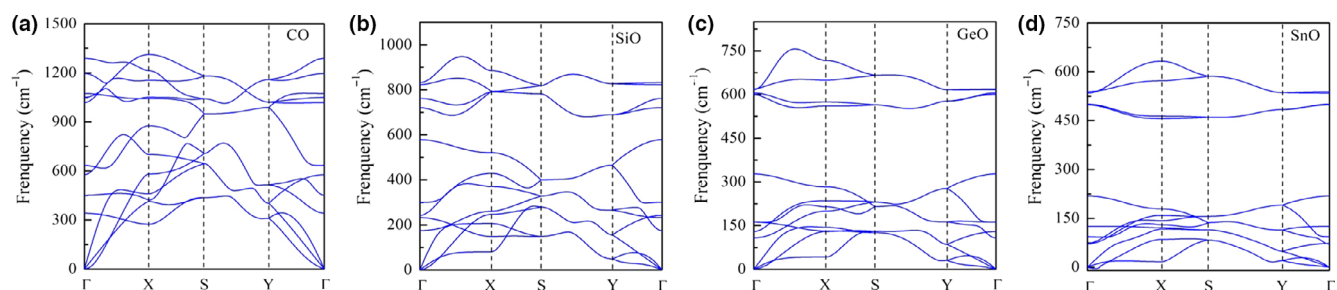


**Figure 2.** Phonon dispersion spectra of Pmma-XO monolayers: a) Pmma-CO, b) Pmma-SiO, c) Pmma-GeO, and d) Pmma-SnO. Reprinted with permission.<sup>[54]</sup> Copyright 2018, IOP Publishing Ltd.

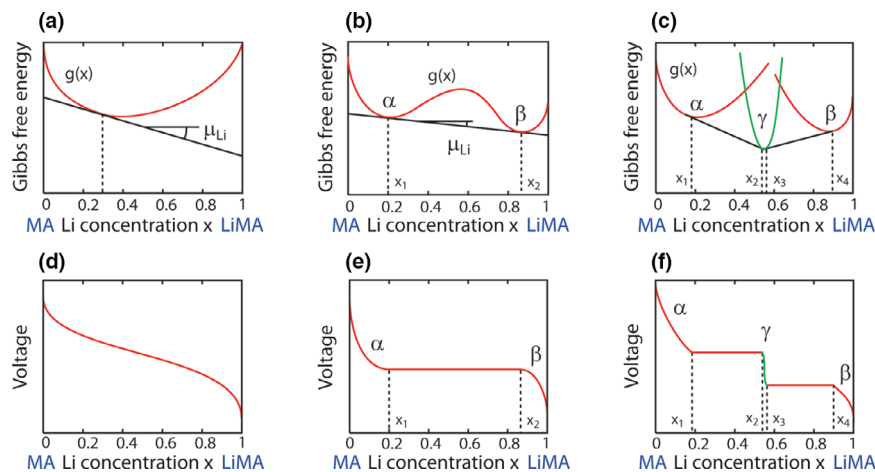


**Figure 3.** Free energy and corresponding voltage profiles with a, d) a solid-phase reaction, b, e) phase transformation from a Li-poor phase to a Li-rich phase, and c, f) the case with a stable intermediate phase. Reprinted with permission.<sup>[56]</sup> Copyright 2012, American Chemical Society.

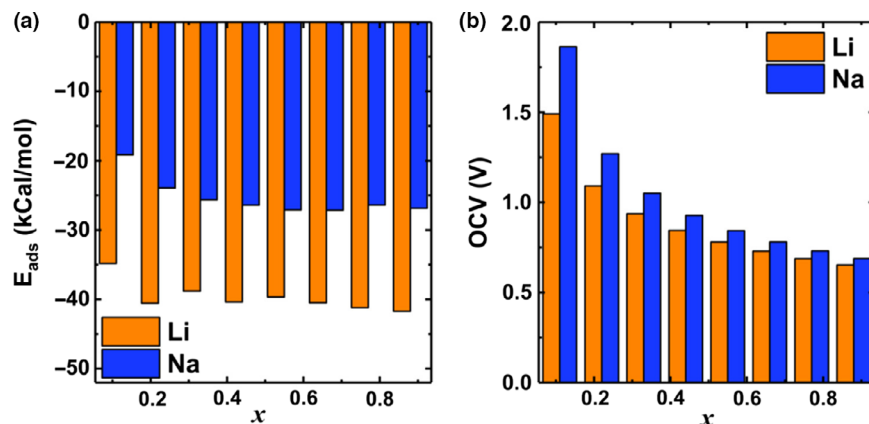


**Figure 4.** a) Calculated adsorption energies per atom, and b) OCVs at different lithiation and sodiation degrees of a 2D AlN. Reprinted with permission.<sup>[40]</sup> Copyright 2018, Elsevier.

### 2.3. Gibbs Free Energy

The Gibbs free energy of a system is defined by the equations below:

$$G = H - TS \quad (3)$$

$$H = E + PV \quad (4)$$

In Equation (3), G, H, S, and T are Gibbs free energy, enthalpy, entropy, and the temperature of the system, respectively. In Equation (4), E, P, and V are the internal energy, pressure, and volume.

Gibbs free energy can be used to compare the stability of isomers or polymorphs at different temperatures or different pressures. In a recent study of the promising cathode material,  $\text{Na}_2\text{FeSiO}_4$ , many different phases were discussed. Owing to the polymorphism of orthosilicate, it is difficult to obtain the single phase to confirm the structure of  $\text{Na}_2\text{FeSiO}_4$  experimentally. Zhu et al. optimized 14 structural models and calculated the free energies under different temperatures and pressures.<sup>[53]</sup> As shown in **Figure 1**, the  $P_n$  phase of  $\text{Na}_2\text{FeSiO}_4$  has the lowest free energy at low temperature and pressure, and it transforms to  $P_n$  when

the temperature reaches  $\sim 700$  °C and to  $\text{Pca}2_1$  when the pressure increases to 8 GPa. These results provide useful guidance for experimentalists in this area.

### 2.4. Phonon Frequency

The phonon spectrum of a structure reflects the collective vibrational mode of all its atoms. If a simulation cell contains  $n$  atoms, the numbers of acoustic branches and optical branches are 3 and  $3n-3$ , respectively. An acoustic branch denotes the vibration of the original cell, and the optical branch describes the relative vibration of the atoms in the cell. An imaginary frequency from the phonon spectrum calculation can be an indicator of the instability of a structure.

Yu-rong An et al. confirmed the structural stability of monolayer structures  $\text{Pmma-XO}$  ( $X = \text{C}, \text{Si}, \text{Ge}$ , and  $\text{Sn}$ ) using phonon dispersion spectra, and these materials are promising polysulfide anchoring materials for LSB.<sup>[54]</sup> As shown in **Figure 2**, there is no imaginary frequency in the phonon dispersion spectra of  $\text{Pmma-CO}$ ,  $\text{SiO}$ , and  $\text{GeO}$ , while negative frequencies appear in the  $\text{Pmma-SnO}$  spectrum around the high symmetry point G. The result shows that  $\text{Pmma-CO}$ ,  $\text{SiO}$ , and  $\text{GeO}$  are dynamically stable, while  $\text{Pmma-SnO}$  is unstable. It should be noted that the highest optical frequencies of  $\text{Pmma-CO}$ ,  $\text{SiO}$ , and  $\text{GeO}$  are  $1200$ ,  $920$ , and  $775$   $\text{cm}^{-1}$ , which are apparently higher than that of 2D black phosphorene ( $\sim 450$   $\text{cm}^{-1}$ ) and  $\text{MoS}_2$  ( $\sim 500$   $\text{cm}^{-1}$ ), indicating a stronger binding property in  $\text{Pmma-CO}$ ,  $\text{SiO}$ , and  $\text{GeO}$  than in phosphorene and  $\text{MoS}_2$ .

Although all of the fore-mentioned four quantities can be used to estimate the stability of a material, they have different areas of applications. The cohesive energy and formation energy are used to evaluate the stability of battery materials at the temperature of absolute 0 K, as we mentioned earlier, formation energy is a better descriptor for this purpose. The Gibbs free energy calculations can be used to compare the stability at different temperatures or pressures, whereas the phonon frequency is computationally demanding and can be only applied for the calculations of small systems or a small part of a large system.

## 3. Reaction Voltage and Theoretical Capacity Prediction

### 3.1. Simulation Principle

In general, the power density of a battery is proportional to the equilibrium voltage, which is an important commercialization index for batteries. DFT calculations can be used to predict the voltage of a new

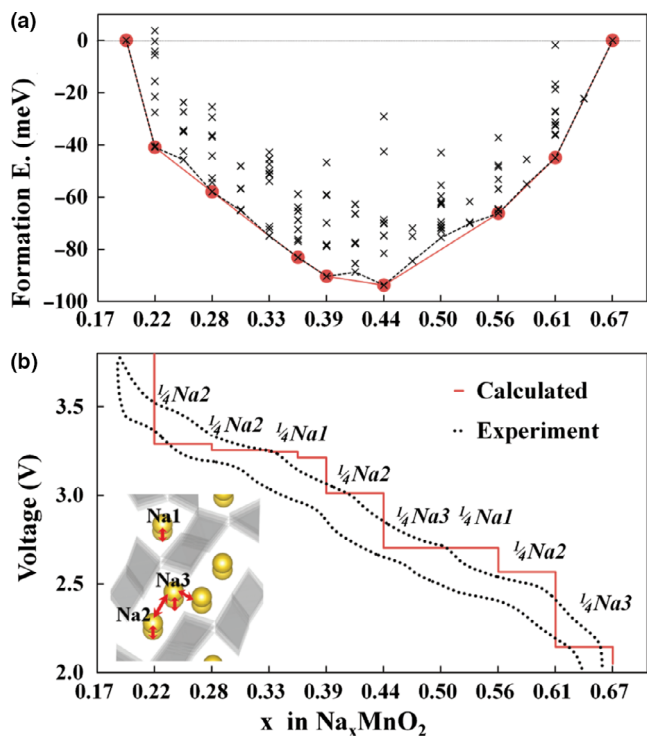


**Figure 5.** a) Comparison of formation energies among seven stable structures at different sodium concentrations during the cycling of  $\text{Na}_x\text{MnO}_2$  in a SIB. b) Voltage profiles in a sodium deintercalation process. The calculated and experimental data are differentiated by red and black lines. The sodium extraction sites for intermediate two-phase reactions are labeled above corresponding voltage plateaus, which are shown at the bottom left of b). Reprinted with permission.<sup>[57]</sup> Copyright 2012, American Chemical Society.

battery system or to analyze the electrochemical reactions in the battery cycling process. A generic electrochemical reaction has the form:



In Equation (5),  $\alpha$ ,  $\beta$ ,  $\gamma$ , and  $\delta$  are stoichiometric coefficients. Under constant temperature and pressure, the Gibbs free energy ( $\Delta_r G^\Theta$ ) of the reaction can be expressed as:

$$\Delta_r G^\Theta = \gamma \Delta_f G_C^\Theta + \delta \Delta_f G_D^\Theta - \alpha \Delta_f G_A^\Theta - \beta \Delta_f G_B^\Theta \quad (6)$$

where the symbol  $\Delta_f G^\Theta$  represents the Gibbs free energy of a specific material. At equilibrium voltage, the reaction is reversible. In a battery,  $\Delta_r G^\Theta$  is equal to the largest nonvolume work that the battery exerts to external systems. If all the Gibbs free energy of the reaction is transformed into electrical energy, the equilibrium voltage can be calculated from the following Nernst equation:

$$\Delta_r G^\Theta = -nFE^\Theta \quad (7)$$

where  $n$  is the mole numbers of ions that transfer in the reaction,  $F$  is the Faraday constant ( $F = 96\,485 \text{ C mol}^{-1}$ ); and  $nF$  represents the total amount of transferred charge;  $E^\Theta$  is the thermodynamic equilibrium voltage under standard conditions, which is also-called

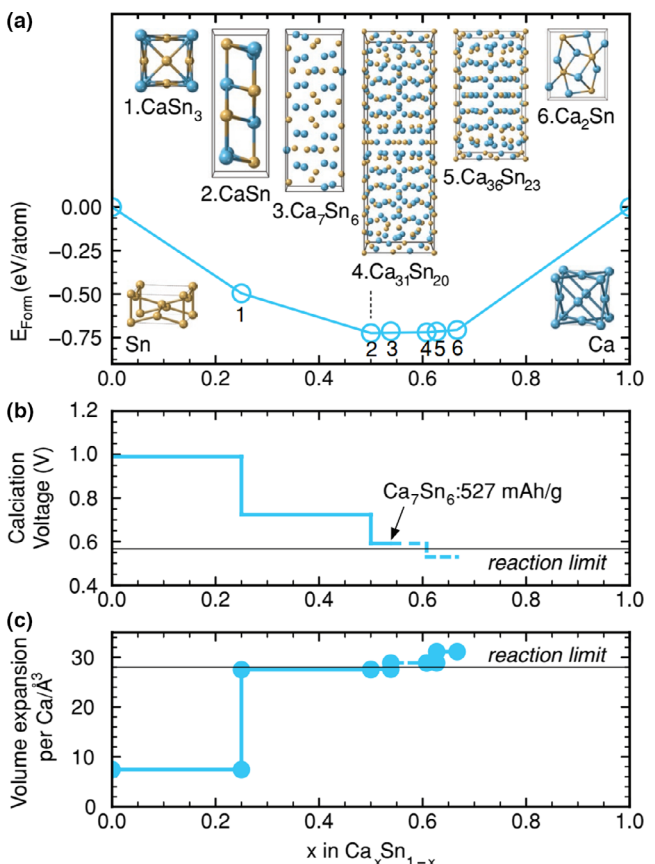


**Figure 6.** a) The formation energy plot of the intermediate products during the calcination of Sn, b) corresponding calcination voltage plot, and c) volume expansion plot per Ca. The structures of reactants and intermediate compounds are shown in the insets in a). Reprinted with permission.<sup>[58]</sup> Copyright 2019, WILEY-VCH Verlag GmbH & Co. KGaA, Weinheim.

electromotive force. According to Equations (3) and (4),  $\Delta G_r^\Theta$  can be written as:

$$\Delta G_r^\Theta = \Delta E_r^\Theta - T\Delta S_r^\Theta + P\Delta V_r^\Theta \quad (8)$$

where  $\Delta E_r^\Theta$  is the energy of reaction, and  $\Delta S_r^\Theta$  is the entropy change. If the system is under constant pressure and at room temperature, the  $P\Delta V_r^\Theta$  and  $T\Delta S_r^\Theta$  terms are negligible.<sup>[55]</sup> Therefore,  $\Delta G_r^\Theta \approx \Delta E_r^\Theta$  is applicable for electrochemical reactions in a battery. The energy of reaction can be calculated with DFT, and the equilibrium reaction voltage can be obtained with Equations (7). Furthermore, the theoretical mass energy density ( $\varepsilon_m$ ), volumetric energy density ( $\varepsilon_v$ ) of a battery, and the specific capacity (C) of an electrode material can be calculated using the following equations:

$$\varepsilon_m = \frac{\Delta_r G^\Theta}{\sum M} \quad (9)$$

$$\varepsilon_v = \frac{\Delta_r G^\Theta}{\sum V} \quad (10)$$

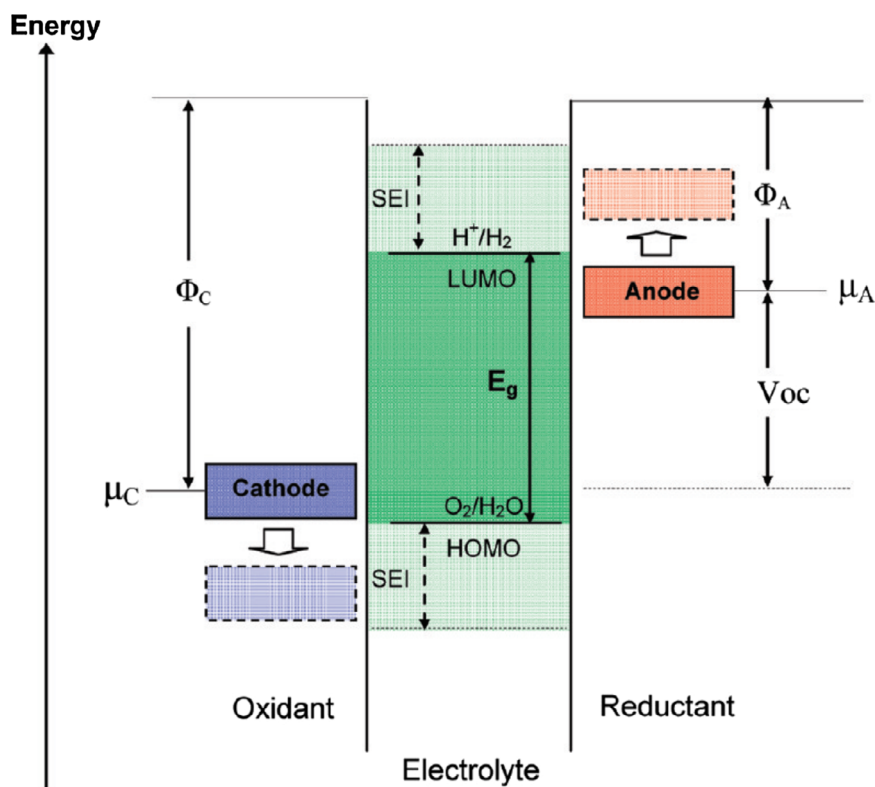


**Figure 7.** Schematic open-circuit energy diagram of an aqueous electrolyte.  $\Phi_A$  and  $\Phi_C$  are the work functions of the anode and cathode, respectively. Reprinted with permission.<sup>[59]</sup> Copyright 2009, American Chemical Society.

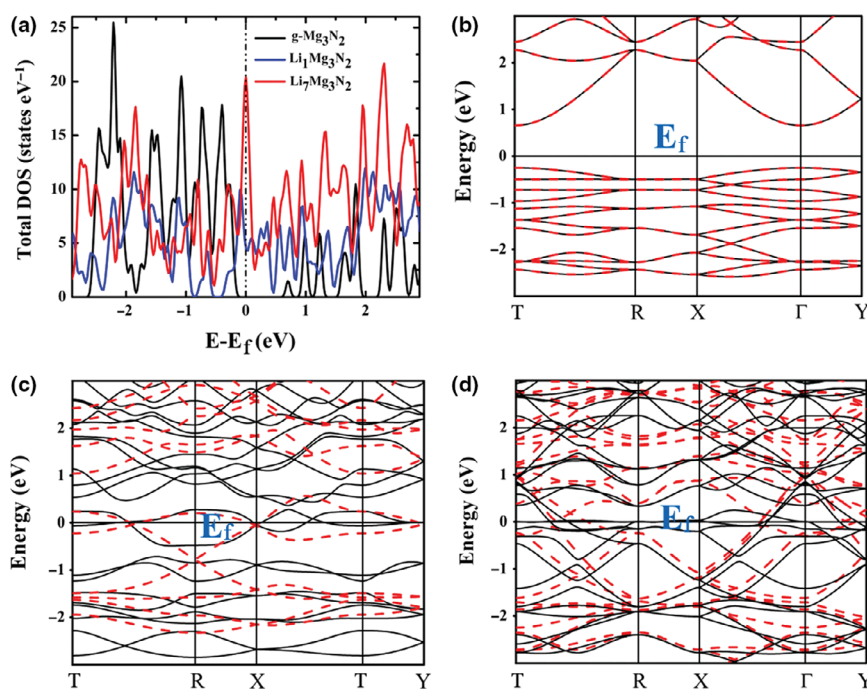


**Figure 8.** a) The total DOSs and b-d) band structures of g-Mg<sub>3</sub>N<sub>2</sub>, LiMg<sub>3</sub>N<sub>2</sub>, and Li<sub>7</sub>Mg<sub>3</sub>N<sub>2</sub>. The Fermi level is aligned to 0 eV. The solid black and dashed red lines are for spin-up and spin-down cases, respectively. Reprinted with permission.<sup>[60]</sup> Copyright 2019, Royal Society of Chemistry.

$$C = \frac{nF}{3.6m} \quad (11)$$

In Equations (9–11), M and V are the sums of mole masses and mole volumes of the reactants (both anode and cathode materials), respectively, and m is the mole mass of an electrode material.

### 3.2. Case Studies

The OCV is the maximum output voltage available for a battery, and it is closely related to the electrochemical reactions occurred inside the battery, which can be measured with the voltage profile experiments. The phase diagram of a battery material and the thermal stability of a specific phase at certain conditions are closely related to the convex hull of the formation energies of the relevant phases, and thus to the voltage profiles. If a lithium metal anode is used as the reference electrode, the Gibbs free energy profile for the intercalation of Li can be elucidated by **Figure 3**. If the electrode material forms a solid solution with intercalated Li, the degree of the freedom of the system is 1 based on the Gibbs phase rules at constant temperature and pressure, as shown in Figure 3a. Accordingly, the voltage is constantly decreasing (Figure 3d). When a first-order phase transformation occurs in a Li-poor phase and a Li-rich phase, the degree of freedom is zero which means the voltage is a constant that is reflected by the plateau in corresponding voltage profile (Figure 3b, e). Additionally, if a stable intermediate phase appears in the lithiation process, there will be multiple plateaus in voltage profiles (Figure 3c, f).<sup>[56]</sup>

Among various electrode materials, the intercalation-type materials generally have stable voltage platforms for battery charging/discharging processes, which correspond to the lithiation/delithiation reactions in batteries. In a recent study<sup>[40]</sup> of lithiation and sodiation properties of 2D AlN, Sengupta et al. calculated the adsorption energies ( $E_{ads}$ ) of lithium/sodium ions on AlN surface and the OCVs at different lithiation/sodiation degrees of the battery. The  $E_{ads}$  is equal to  $\Delta E_r^\Theta$  and approximate to  $\Delta G_r^\Theta$  in Equation (8) for this particular case. The calculations were performed with the PBE exchange-correlation functional and the norm-conserving Troullier-Martins pseudopotential. The results are presented in **Figure 4**, which shows that, with an increase of the level of lithiation/sodiation, the OCVs decrease synchronously. Interestingly, at the same intercalation states of the 2D AlN anodes, the SIBs always show higher OCVs than

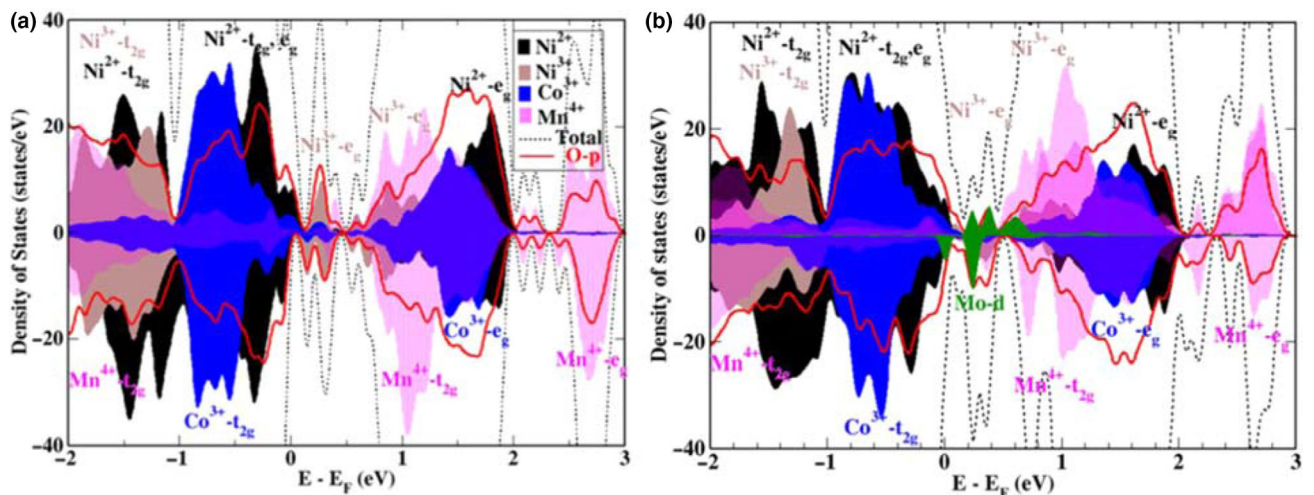


**Figure 9.** Density of states for a) undoped, b) Mo-doped, and b) NCM523 samples. Reprinted with permission.<sup>[29]</sup> Copyright 2018, American Chemical Society.

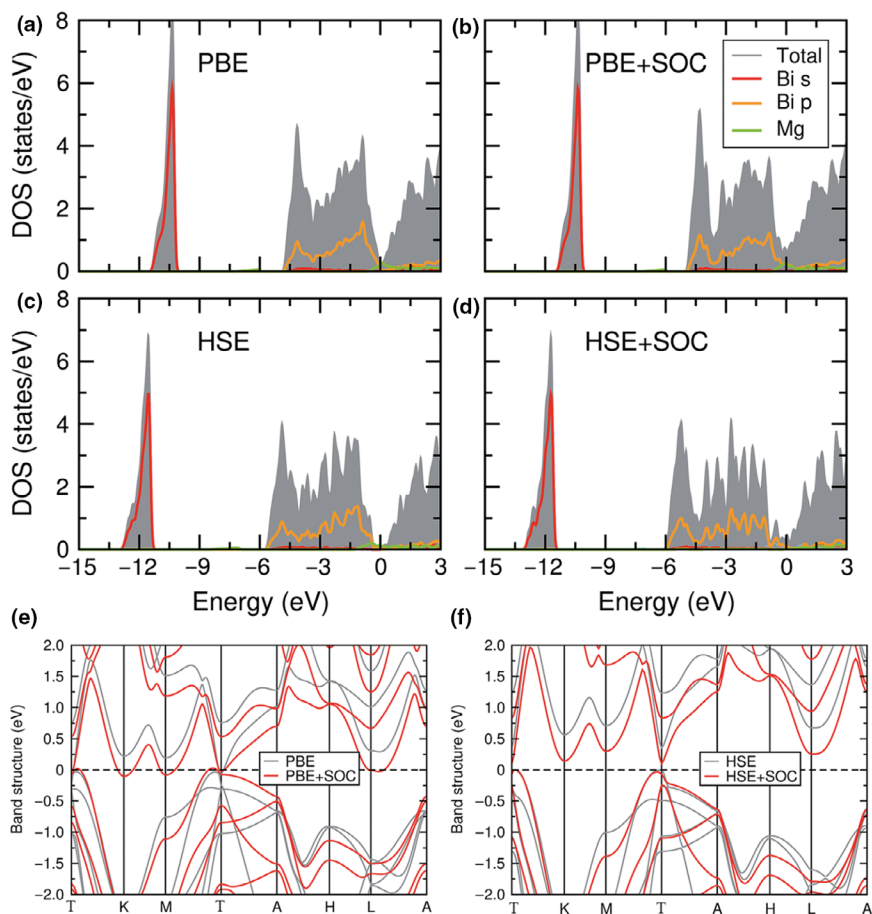


**Figure 10.** a-d) The DOS and e-f) the band structure plots of  $Mg_3Bi_2$  calculated using PBE and HSE06 exchange-correlation functionals with/without SOC. Local atomic DOS projections inside the sphere are defined by the Wigner-Seitz radii (1.63 and 1.52 Å for Bi and Mg, respectively). Reprinted with permission.<sup>[44]</sup> Copyright 2018, Royal Society of Chemistry.

that of LIBs, which indicates that it is easier for Na ions to be adsorbed in AlN. Overall, the calculated OCVs demonstrate the potential applicability of the 2D AlN anode in LIBs and SIBs.

In the electrochemical reactions, the intermediates produced at different charging/discharging stages may be metastable phases. The  $Na_{0.44}MnO_2$  material was systematically investigated by Kim et al.,<sup>[57]</sup> and it forms seven stable intermediate phases in the cycling process (Figure 5). The corresponding sodium deintercalation voltages were calculated using the GGA+U method, and the results are consistent with experiments. Their calculations reveal the exact sodium extraction sites, which clearly reflect the reaction kinetics of  $Na_{0.44}MnO_2$  in SIBs. Based on the theoretical calculations, they found that the capacity fading at low potentials is due to the high diffusion barrier of Na ions.

Recently, Yao et al.<sup>[58]</sup> carried out a theoretical calculation of the calcination process of a Sn anode in CIB. Figure 6 shows the Sn-Ca convex hull, the corresponding formation energies, calcination voltages, and volume expansions, and six intermediate products were taken into consideration. As the calcination voltage threshold was defined as 0.53 V, there are no reactions occur below 0.53 V. The final reaction product is  $Ca_7Sn_6$ , which corresponds to a theoretical capacity of 527 mAh g<sup>-1</sup>. According to their calculations, the actual calcination process of Sn follows the path:  $Sn \rightarrow CaSn_3 \rightarrow CaSn \rightarrow Ca_7Sn_6$ , and the calcination voltages of these

three steps are 0.99, 0.72, and 0.59 V, respectively. From the Sn-Ca convex hull, it is worth noting that the transformations of Sn to CaSn<sub>3</sub> and CaSn<sub>3</sub> to CaSn are accompanied by a long plateau, indicating that a large amount of Ca participate in the reactions. Besides the

calculations for the Sn anode, the Zn, Li, and Na anode were theoretically analyzed with the calcination voltage threshold of 0.53V. The results show that the calcination of Zn should end at CaZn<sub>5</sub>, whereas Li and Na have poor calcination performance. According to these findings,

the authors carried out high-throughput DFT calculations to search promising anodes for CIB. They found that some nonmetals, including Si, Sb, and Ge, and transition metals Al, Pb, Cu, Cd, and CdCu<sub>2</sub> are potential anode materials for CIB.

## 4. Electronic Structure

The electronic structure of an electrode or electrolyte material plays an important role on the performance of a battery. Since all DFT calculations are based on the electron density, the electronic structure of battery materials can be routinely obtained with DFT calculations, including molecular orbitals, band structure, density of state, and charge distribution, and these properties can help the users analyze the performance of battery materials.

### 4.1. Molecule Orbitals

The selection of electrolyte materials for batteries must meet some specific rules, such as low-toxicity, low-cost, low-electronic conductivity, and high ionic conductivity, and noninflammability. A good battery design should avoid chemical reactions occurred in the electrolyte. In 2010, Goodenough<sup>[59]</sup> proposed that an eligible electrolyte should possess a large potential window with the highest occupied molecular orbital (HOMO) lower than the Fermi level of the cathode ( $\mu_C$ ), and the lowest occupied molecular orbital (LOMO) higher than the Fermi level of the anode ( $\mu_A$  in **Figure 7**). The electrolyte will be reduced if the  $\mu_A$  is higher than LUMO, and it will be oxidized when the  $\mu_C$  is lower than HOMO. Fortunately, this problem can be mitigated if there is a stable solid electrolyte interface (SEI) formed to prevent the electrons transferring between electrodes and electrolyte. DFT can be employed to calculate the HOMO/LUMO energetics in the electrolyte candidates, which can be used for examining the compatibility of an electrolyte with specific anode and cathode materials.

### 4.2. Band Structures

In solid-state physics, the electronic band structure provides the information about the range of energy levels an electron within the solid

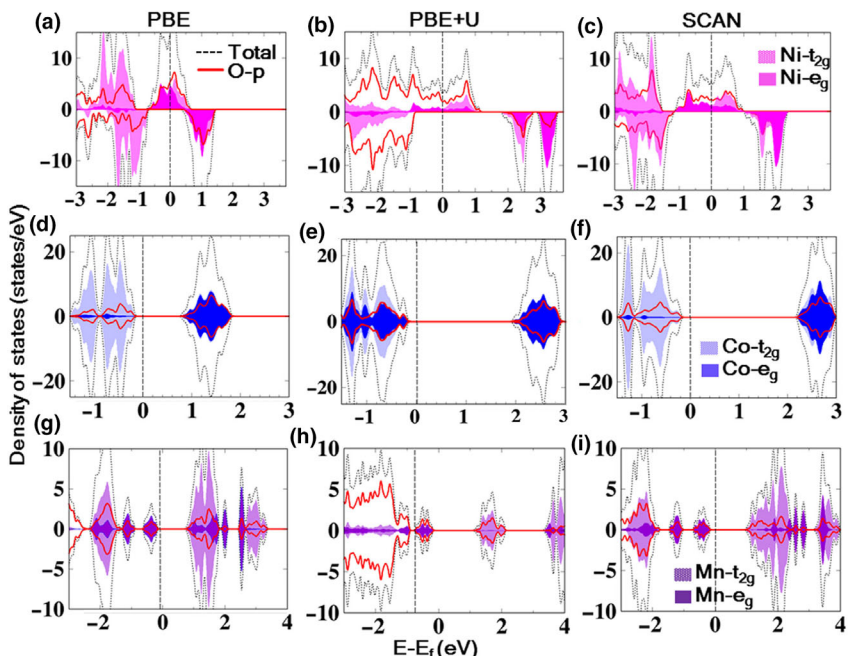


**Figure 11.** a–c) DOSs of LiNiO<sub>2</sub>, d–f) LiCoO<sub>2</sub>, and g–i) LiMnO<sub>2</sub> obtained using PBE, PBE+U, and meta-SCAN functionals.<sup>[61]</sup> Copyright 2018, Nature.

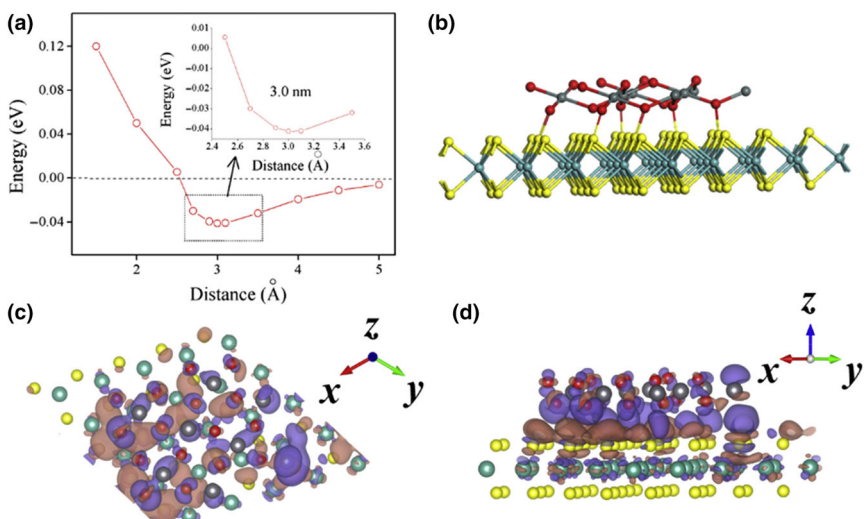


**Figure 12.** a) Adsorption energy of SnO<sub>2</sub> on the MoSe<sub>2</sub> (1 0 0) plane as a function of Se-O band lengths. b) Geometrically optimized structure of SnO<sub>2</sub>-MoSe<sub>2</sub> interface. c, d) Top and side views of the charge density difference of the SnO<sub>2</sub>-MoSe<sub>2</sub> interface; the brown and purple bubbles represent charge accumulation and depletion, respectively. (Isosurface level = 0.000605 e bohr<sup>-3</sup>) Reprinted with permission.<sup>[34]</sup> Copyright 2018, Elsevier.

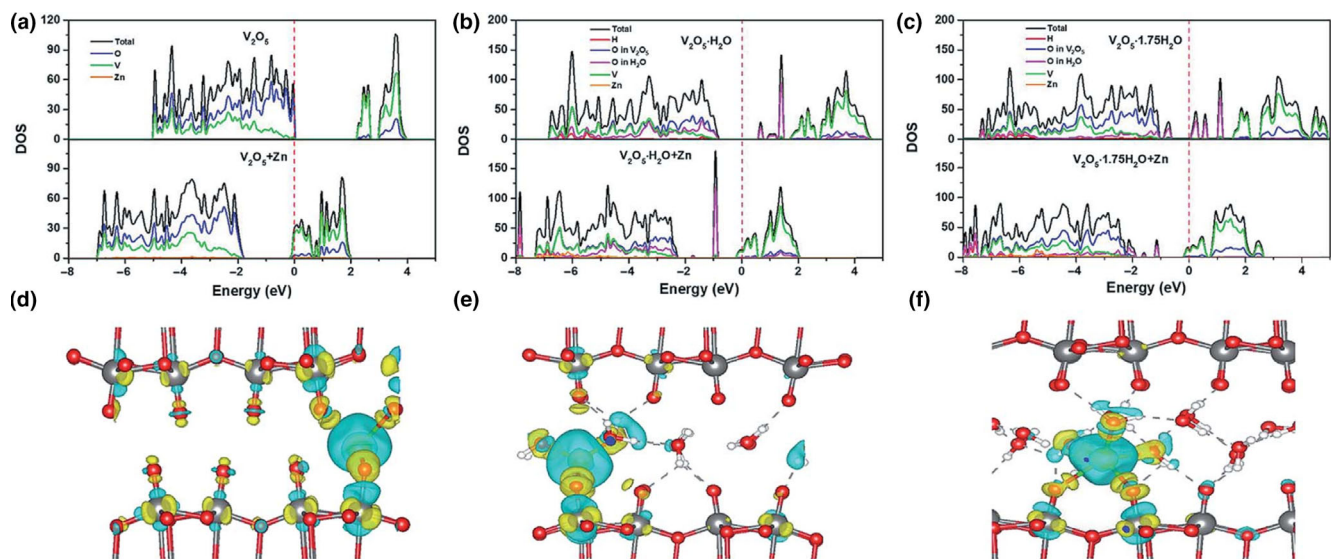


**Figure 13.** The DOSs of a)  $\text{V}_2\text{O}_5$  and  $\text{V}_2\text{O}_5 + \text{Zn}$ , b)  $\text{V}_2\text{O}_5 \cdot \text{H}_2\text{O}$  and  $\text{V}_2\text{O}_5 \cdot \text{H}_2\text{O} + \text{Zn}$ , c)  $\text{V}_2\text{O}_5 \cdot 1.75\text{H}_2\text{O}$  and  $\text{V}_2\text{O}_5 \cdot 1.75\text{H}_2\text{O} + \text{Zn}$ . The red line represents the location of the Fermi level. d–f) The deformation charge densities of  $\text{V}_2\text{O}_5 + \text{Zn}$ ,  $\text{V}_2\text{O}_5 \cdot \text{H}_2\text{O} + \text{Zn}$  and  $\text{V}_2\text{O}_5 \cdot 1.75\text{H}_2\text{O} + \text{Zn}$ , respectively. The gray dash line represents the hydrogen bond, and the isosurface value is  $0.005 \text{ e bohr}^{-3}$ . Reprinted with permission.<sup>[62]</sup> Copyright 2019, Royal Society of Chemistry.

can occupy, and the band gap is closely related to the electronic conductivity. From a recent DFT study, Xiong et al. predicted that  $\text{Mg}_3\text{N}_2$  is a potential high-performance anode material for LIBs owing to its stable structure and high theoretical capacity, proper intercalation potential, and a low ion transport barrier.<sup>[60]</sup> **Figure 8** shows the DOSs and band structures of the original and lithiated  $\text{Mg}_3\text{N}_2$  materials. Their calculations revealed that the pristine  $\text{Mg}_3\text{N}_2$  has a band gap of only 0.91 eV (PBE), indicating that it is a semiconductor. After the intercalation of Li ions, the intermediate,  $\text{LiMg}_3\text{N}_2$ , and the final product,  $\text{Li}_7\text{Mg}_3\text{N}_2$ , are metallic with no band gaps, which means that the lithiation process enhances the electronic conductivity of  $\text{Mg}_3\text{N}_2$ . Since the PBE functional tends to underestimate the band gaps, the HSE06 hybrid functional has been employed to recalculate the band gaps. As expected,

the HSE06 band gap of  $\text{Mg}_3\text{N}_2$  is 1.92 eV, about 1 eV higher than that of PBE. However, the lithiated  $\text{Mg}_3\text{N}_2$  species have been shown to be metallic even with the HSE06 functional. Based on these electronic structure analyses,  $\text{Mg}_3\text{N}_2$  is shown to have good electronic conductivity and good rate capacity during the cycling process.

#### 4.3. Density of States

The DOS is essentially the number of different states at a particular energy level that electrons are allowed to occupy, that is, the number of electron states per unit volume per unit energy. From a recent DOS analysis, Breuer et al.<sup>[29]</sup> confirmed that the doping of  $\text{Mo}^{6+}$  in  $\text{LiNi}_{0.5}\text{Co}_{0.2}\text{Mn}_{0.3}\text{O}_2$  (NCM523) can affect its electronic structure and thus its electrochemical performance in LIBs. The calculated DOS of undoped and Mo-doped NCM523 are shown in

**Figure 9**. Although the DOSs do not change significantly after Mo doping, the increase of  $\text{Ni}^{2+}$  partial DOS (PDOS) and the corresponding decrease of  $\text{Ni}^{3+}$  PDOS demonstrate the charge compensation of  $\text{Ni}^{3+}$ . Furthermore, the conduction bands of  $\text{Mo}^{6+}$  near the Fermi level increase the conductivity of NCM523 based on the computational and experimental results, and the position of Mo PDOS also explains the appearance of  $\text{Mo}^{5+}$  and  $\text{Mo}^{6+}$  during battery cycling.

The band gap of a material directly relates to its conductivity, and the electronic resistance of electrode materials can be analyzed using DOS plots. Lee<sup>[35]</sup> calculated the DOSs of the composite of polymeric graphitic carbon nitride (pg-CN) and amorphous carbon black (a-CB) and their individual DOSs. It turns out that the band

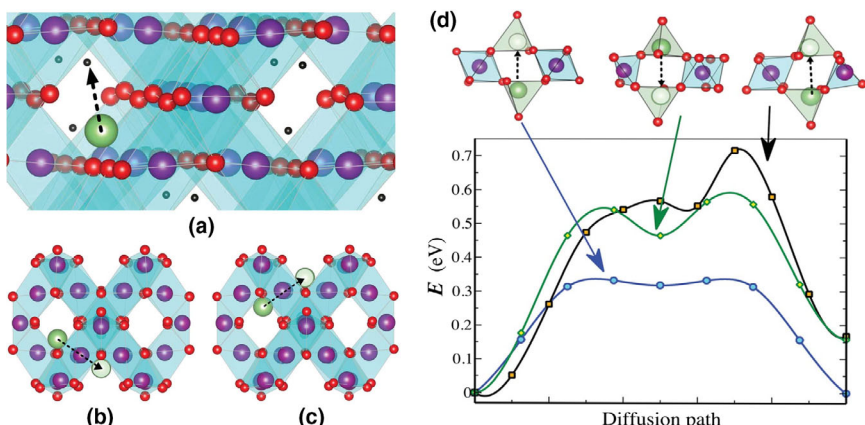


**Figure 14.** Diffusion paths (indicated by dashed arrows) followed by a Li ion inside the internal cubic structures of spinel LMO of different sizes: a) 14 nm (bulk); b,c) 1.3 nm (nanoparticle). The black points in a) are positions of minimum energy that can be occupied by Li ions. d) Energy barrier profiles along the Li-ion diffusion paths in bulk LMO a) and nanosized LMO b,c), which are drawn with the blue, green, and black lines, respectively. Reprinted with permission from ref.<sup>[32]</sup> Copyright 2018 Royal Society of Chemistry.

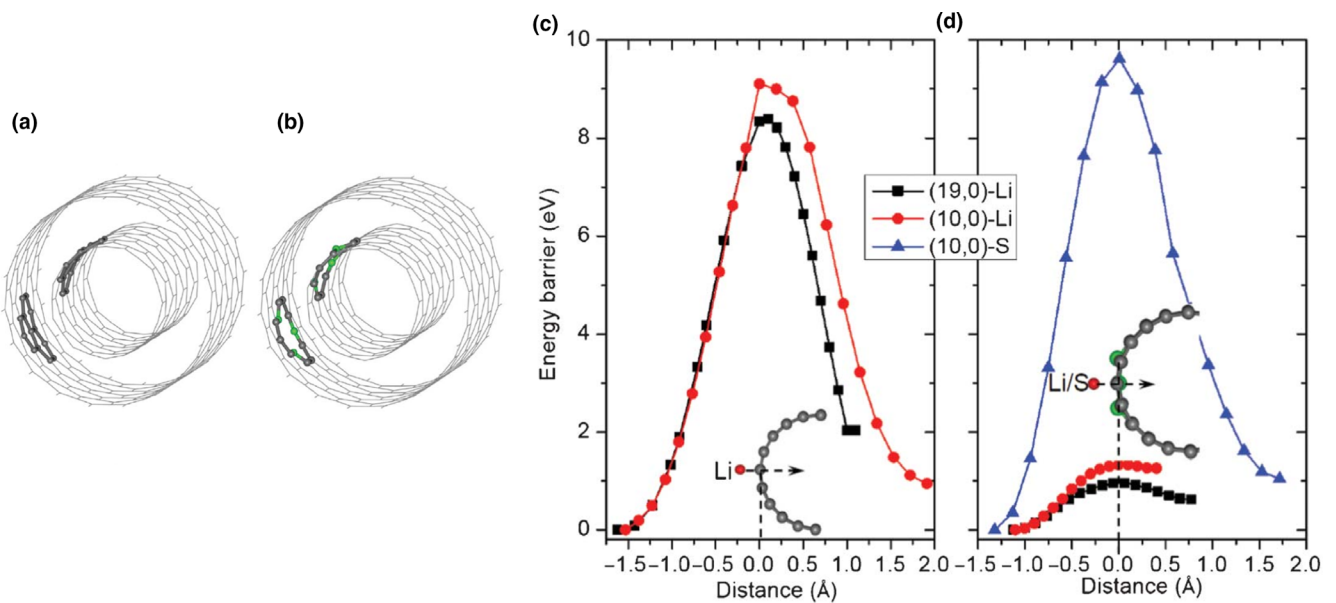


**Figure 15.** Atomic configurations of a) perfect and b) pyridinic N-doped zigzag double-walled CNTs. c) Energy profiles of the Li atom's penetrations through the outer wall and inner wall of perfect CNTs. d) Energy profiles of the Li and S atom's penetrations through the outer wall and inner wall of N-doped CNTs. Reprinted with permission.<sup>[64]</sup> Copyright 2018, Royal Society of Chemistry.

gap of pg-CN is 2.0 eV, while a-CB and the a-CB/pg-CN composite have no band gaps. The result verifies that the strategy of encapsulating the original a-CB with a layer of pg-CN can enhance structural stability without lowering its electronic conductivity.

Recently, DFT has been employed in the studies of the emerging MIB materials, and Lee et al.<sup>[44]</sup> calculated the DOS and band structure of Mg<sub>3</sub>Bi<sub>2</sub>, a potential MIB anode material with a good rate performance, using the semilocal PBE and hybrid HSE06 functionals (Figure 10). Both PBE and HSE06 calculations show that the top of the valence band almost totally originates from the Bi 6p orbitals. The large gaps between the top of Bi 6s and the bottom of Bi 6p demonstrate the chemical inertness of Mg<sub>3</sub>Bi<sub>2</sub>. Since PBE usually underestimates the band gaps of solids, PBE gives no band gaps for Mg<sub>3</sub>Bi<sub>2</sub> with or without spin-orbit coupling (SOC), whereas HSE06 gives a band gap of 0.36 eV for Mg<sub>3</sub>Bi<sub>2</sub>. Their assessments show that SOCs reduce the band gap and increase the dispersion of Bi 6p, and it should be taken into consideration in the calculations of the systems containing heavy atoms.

DOSs can be used to calculate the electron occupation states, and Chakraborty et al. adopted the SCAN meta-GGA density functional to calculate the structural, magnetic and electrochemical properties of layered transitional oxides, including LiNiO<sub>2</sub>, LiCoO<sub>2</sub>, and LiMnO<sub>2</sub>, which are commercial cathode materials for LIBs.<sup>[61]</sup> The DOSs of these compounds were compared in Figure 11, and it shows that the Ni, Co, Mn-d, and O-p states have distinctive hybridization, indicating the strong binding of the transition metal atoms with oxygen atoms. In addition, the metal-d states give significant contributions to the valence bands near the Fermi level. Furthermore, the Ni<sup>3+</sup> in LiNiO<sub>2</sub> and the Co<sup>3+</sup> in LiCoO<sub>2</sub> are in the low-spin state ( $t_{2g}^6$  ( $\uparrow\downarrow\uparrow\downarrow\uparrow\downarrow$ ),  $e_g^0$  ( $\mid\mid$ )), which means that both the up and down  $t_{2g}$  spin channels are completely occupied. In contrast, the Mn<sup>3+</sup> in LiMnO<sub>2</sub> is in a high-spin state ( $t_{2g}^3$  ( $\uparrow\uparrow\uparrow\uparrow\mid$ ),  $e_g^1$  ( $\uparrow\mid\mid$ )). The results based on the meta-GGA functional were compared with those obtained using PBE+U and PBE functionals. From their comparison, we can see that the PBE+U

functional underestimates the energy of the metal-d states near the Fermi level, whereas SCAN gives a more accurate prediction, and PBE+U tends to overestimate the energy of the O-p states.

#### 4.4. Electronic Distribution

A popular form of showing electronic structure is the electronic/charge distribution obtained from the DFT calculations. Charge distribution patterns clearly show the electronic structures of the electrode materials and the chemical environment of the atoms, which are difficult to be measured by experiments. Zhao et al.<sup>[34]</sup> simulated a lamellar MoSe<sub>2</sub>-SnO<sub>2</sub> interface and calculated the charge density of the interface (Figure 12). The charge density difference of the MoSe<sub>2</sub>-SnO<sub>2</sub> interface was computed by subtracting the individual charge densities of MoSe<sub>2</sub> and SnO<sub>2</sub> from that of the MoSe<sub>2</sub>-SnO<sub>2</sub> interface. Figure 12c, d illustrates the transfer of electrons after the adsorption of SnO<sub>2</sub> on MoSe<sub>2</sub>. The Se atoms on the MoSe<sub>2</sub> surface lose electrons, which transfer toward O atoms of SnO<sub>2</sub>, and the charge density between Se and O atoms on the surface increases, corresponding to the formation of chemical bonds between Se and O, which is also proved in Figure 12a. When the electrons depart from nuclei, the constraint of electrons from the nuclei is weakened, and thus the mobility of electrons is significantly enhanced. Therefore, the electron conductivity of MoSe<sub>2</sub> can be strikingly improved by the doping of SnO<sub>2</sub>, and the lamellar MoSe<sub>2</sub>-SnO<sub>2</sub> shows high rate capacity in SIBs.

Recently, Wu et al.<sup>[62]</sup> reported a study of the bilayer structured V<sub>2</sub>O<sub>5</sub>•nH<sub>2</sub>O as the cathode material for aqueous ZIBs, and they investigated the electronic structures of V<sub>2</sub>O<sub>5</sub>•nH<sub>2</sub>O with intercalation of Zn<sup>2+</sup> through charge density distribution and DOS. Figure 13 shows the calculated DOSs and deformation charge densities of the pristine and the Zn<sup>2+</sup> intercalated V<sub>2</sub>O<sub>5</sub>•nH<sub>2</sub>O structures. For V<sub>2</sub>O<sub>5</sub> without the bonded H<sub>2</sub>O, a tremendous amount of electrons from Zn transfer to the neighbor V and O. However, with the bonded H<sub>2</sub>O, V<sub>2</sub>O<sub>5</sub>•H<sub>2</sub>O for instance,

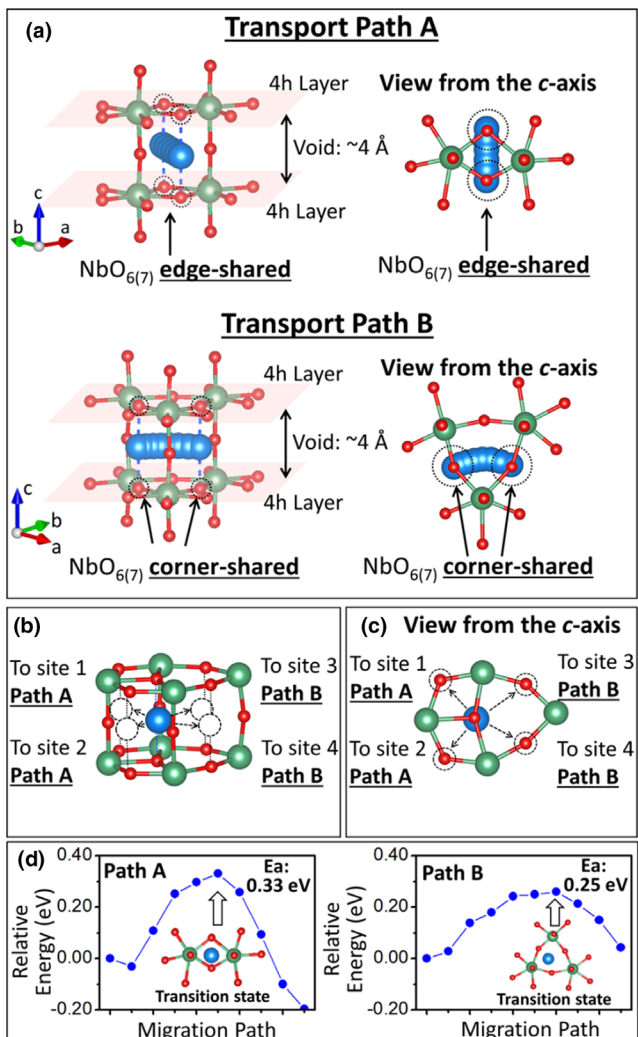


**Figure 16.** a) Two transport pathways of Li inside  $\text{Nb}_2\text{O}_5$ . b,c) The possible neighboring sites to which the Li ions may migrate. d) Transport energy profiles of Li along path A and B listed in a). Reprinted with permission.<sup>[37]</sup> Copyright 2017, American Chemical Society.

the charge transferring orientation changes. Except for moving from Zn to V and O, the electrons mainly exchange between Zn and  $\text{H}_2\text{O}$ . The results are confirmed by comparing the changes of DOSs of  $\text{V}_2\text{O}_5 \cdot \text{H}_2\text{O}$ , which show that the DOSs move to lower energy section after the  $\text{Zn}^{2+}$  intercalation, indicating that the electrons of Zn transfer to the conduction band. To quantify the number of transferred electrons, the authors calculated the Bader charges, and the results show that a large portion of electrons originating from Zn were acquired by V in  $\text{V}_2\text{O}_5$ , while the electrons mainly move to the oxygen atoms of  $\text{H}_2\text{O}$  in  $\text{V}_2\text{O}_5 \cdot \text{H}_2\text{O}$  and  $\text{V}_2\text{O}_5 \cdot 1.7\text{H}_2\text{O}$ . Therefore, the bonded  $\text{H}_2\text{O}$  has a significant effect on the electrochemical performance of  $\text{V}_2\text{O}_5 \cdot \text{nH}_2\text{O}$  in ZIBs.

## 5. Ions/molecules Transport Kinetics

Apart from the reaction voltage, it is very instructive to investigate the processes of ion diffusion occurring at atomic scale within batteries. It is well known that ionic diffusivity plays a pivotal role for the

performance of electrode materials, and it is closely related to the electrochemical properties of batteries such as rate capability, cycling performance, and structural stability.<sup>[31]</sup> DFT has been employed to simulate the transport mechanism of ions in batteries by calculating the activation energy along the ions diffusion paths.<sup>[32,40]</sup> The nudged elastic band (NEB) method and modified climbing image nudged elastic band (CI-NEB) method are commonly used to simulate the diffusion kinetics.<sup>[63]</sup>

Velasquez et al.<sup>[32]</sup> reported that when the nanoparticles of  $\text{LiMn}_2\text{O}_4$  (LMO) is less than a certain critical average size ( $\sim 15$  nm), the smaller sized LMO electrode materials lead to worse battery performances, which contradicts the popular trend in the community of LIBs. In order to understand the rare phenomenon occurring inside the small nanoparticles, DFT and the NEB method were employed to calculate the energy barriers for Li-ion diffusion inside the spinel structural LMO nanoparticles of different average sizes (illustrated in Figure 14). The calculated energy barrier profiles for a Li ion along three different diffusion paths are shown in Figure 14d. The maximum diffusion energy barrier for the Li-ion diffusion in a bulk LMO particle (blue line in Figure 14d) is 0.33 eV. As for nanosized LMO particles (green and black lines in Figure 14d), there exist two possible Li-ion diffusion paths, for which the highest energy barriers are 0.59 and 0.72 eV, respectively. The DFT calculations show that, as the size of LMO nanoparticles changing from 14 to 1.4 nm, the corresponding energy barrier of Li-ion diffusion increases from 0.33 to at least 0.59 eV. The series of calculations shed lights on the reason that a smaller size of LMO nanoparticles causes an increased hindrance for the Li-ion extraction/insertion processes, resulting an increased redox voltage.

In a recent paper, Wang et al. have shown that nitrogen-doped carbon nanotube (CNTs) is a high-performance cathode host material in LSBs.<sup>[64]</sup> In this study, DFT was employed to investigate the diffusion of Li ions through the outer surface, inner surface, and inter-wall spaces of CNTs. Figure 15 gives the atomic configurations of the perfect and the N-doped CNTs, and the calculated energy barrier profiles along Li-ion diffusion pathways from the outer wall to the inner wall in the pristine and N-doped CNTs. For the perfect CNTs, the energy barriers for the migrations of Li atoms through the outer and inner walls are about 8.4 and 9.1 eV, respectively, which are much higher than those of N-doped CNTs (about 0.95 and 1.33 eV, respectively). Furthermore, it can be seen that S atoms are encapsulated in the N-doped CNTs because of the high diffusion energy barrier of 9.6 eV. Therefore, the results demonstrate the potential utilization of the N-doped CNTs as the cathode host material in high-performance LSBs.

In a recent study of  $\text{Nb}_2\text{O}_5$ , DFT has been employed to investigate the Li-ion diffusion mechanism in the orthorhombic  $\text{Nb}_2\text{O}_5$ .<sup>[65]</sup> Based on the structure of orthorhombic  $\text{Nb}_2\text{O}_5$ , Chen et al.<sup>[37]</sup> classified the diffusion paths into two categories (path A and B listed in Figure 16). Both paths provide the room for Li-ion diffusion with very little steric hindrance from Nb or O atoms. The migration energy barriers for the diffusion of the Li ion to neighboring sites are small, which are competitive to the most advanced Li-ion conductors. Along the selected pathways, the energy barrier of each step was calculated. As the energy profiles (Figure 16d) shown, the diffusion energy barriers of Li ion along the path A and B are 0.33 and 0.25 eV. In this study, the authors confirmed that the anomalous fast ionic conductivity of orthorhombic  $\text{Nb}_2\text{O}_5$  is ascribed to its intrinsic structure, and this is a successful story of the prediction of the ionic conductivity through DFT calculations.

Ab initio molecular dynamics (AIMD) is another useful tool to investigate the ion transport kinetics.<sup>[66]</sup> Contrast to the classic MD, the

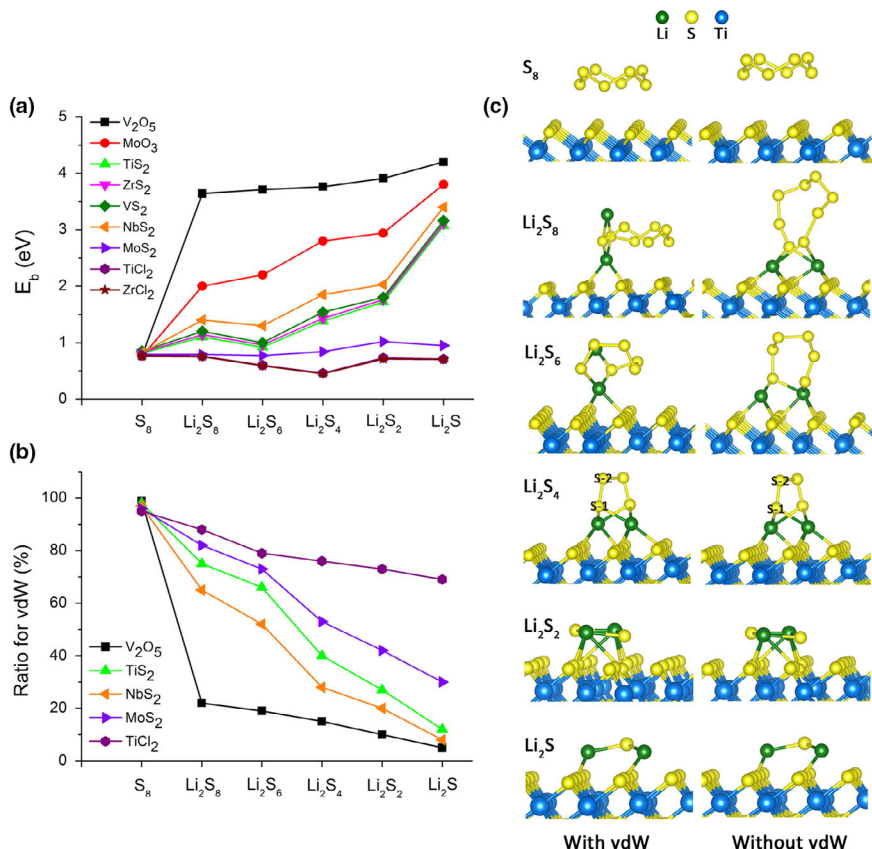


**Figure 17.** a) Binding energies of different polysulfides on different anchor materials. b) Ratios of vdW interaction for five selected anchor materials. c) Stabilized conformations of different polysulfides adsorbed on the surface of  $TiS_2$  with/without vdW. Reprinted with permission.<sup>[71]</sup> Copyright 2015, American Chemical Society.

forces in AIMD can be obtained by the DFT calculations, and AIMD is more accurate in quantifying the diffusion properties. However, AIMD requires much more computational resources and can only handle the systems of several hundred atoms if the diffusion is reasonably fast. The NEB method only gives the energy barrier for a migration pathway, but AIMD can further provide the diffusion coefficient and ionic conductivity, which can be verified by experiments.

## 6. Adsorption Kinetics

In the electrochemical reactions of battery materials, the adsorption of ions plays a key role on the reactivity of the electrode materials, so the adsorption kinetics has great influence on the capacity and cycling performance of batteries. Tremendous research efforts in LSBs are devoted to solving the so-called “shuttle effect.” An effective and popular approach is to adopt a sulfur host that can tightly anchor the soluble polysulfides.<sup>[67–70]</sup> In principle, the adsorption energy can be calculated with DFT, and the calculations can be employed to quantify the performance of the designed battery materials. In order to solve the “shuttle effect” problem, Cui’s group compared the adsorption energies of a series of 2D potential sulfur hosts, including oxides, sulfides, and chlorides (Figure 17),<sup>[71]</sup> and the adsorption energies of polysulfides at different lithiation states were calculated in order to

obtain the trend of anchoring effect. As shown in Figure 17a, the binding strengths of polysulfides with all of the tested 2D materials roughly increase during the lithiation process, except  $ZnCl_2$ . From the comparisons,  $V_2O_5$  and  $MoO_3$  have been shown to have strongest anchoring effect to polysulfides and these DFT results can give good guidance in search of the efficient sulfur host materials. In addition, the contribution of the van der Waals (vdW) interaction of several anchor materials was analyzed in their DFT calculation, and they found that the physical adsorptions gradually transform into chemical bonding to polysulfides with the progressing of lithiation. This observation suggests that the vdW correction should be included in the DFT calculations when measuring the interactions between polysulfides and 2D anchor materials.

The adsorption of Li ions on the surface of the LIB electrodes contributes partially to the storage of Li ions. Spinel  $ZnFe_2O_4$ , as an anode with a high theoretical capacity, shows a high-voltage plateau in initial discharging process. However, this plateau behavior cannot be explained by the general Li-ion intercalation, and the reason behind this phenomenon remained unclear until Guo et al.<sup>[72]</sup> reported their DFT mechanistic study. In their calculations, the DFT + U method was employed to calculate the adsorption energies of Li ions on different surfaces of  $ZnFe_2O_4$  (Figure 18). The binding energies of Li ions on different adsorption sites at different Li-ion concentrations

were calculated to find the most active adsorption sites and the Li storage capacities. Both O and Zn-terminated (111) surfaces have stronger attractive interaction with Li ions than the  $ZnFeO_2$ -terminated (110) surfaces, and the binding energies increase when more Li ions are adsorbed on the surfaces. These results demonstrate the effective storage of Li on  $ZnFe_2O_4$  (111) surfaces. Furthermore, the calculations and experiments confirm that the initial high discharging potential originates from the adsorption of Li ions on the Zn-terminated  $ZnFe_2O_4$  (111) surface.

The silicon-based anode materials for LIBs have high specific capacities, but there are two major hindrances for their practical applications: 1) the large volume changes of Si during charging/discharging processes and 2) the low conductivity. Loading Si onto N-doped graphene (NG) has been shown to be effective in improving the conductivity and relieving the volume-changing effect. In addition, NG increases the amount of adsorbed Li, which was confirmed by Zou et al.<sup>[73]</sup> in a recent DFT study. They found that the  $Si_2$ ,  $Si_3$ , and  $Si_6$  clusters have strong binding with NG, with the  $Si_6$  cluster having the shortest Si-C bond length. The most active adsorption site is the C atom surrounded by N atoms. The adsorption energies of Li on different  $Si_6$ /NG hybrid structures with different numbers of Li atoms were calculated (Figure 19). The pyrrolic N shows more positive effects on adsorbing Li ions than the pyridinic N, even though both show strong adsorption capability for Li ions. Furthermore, the adsorption energies of single Li are

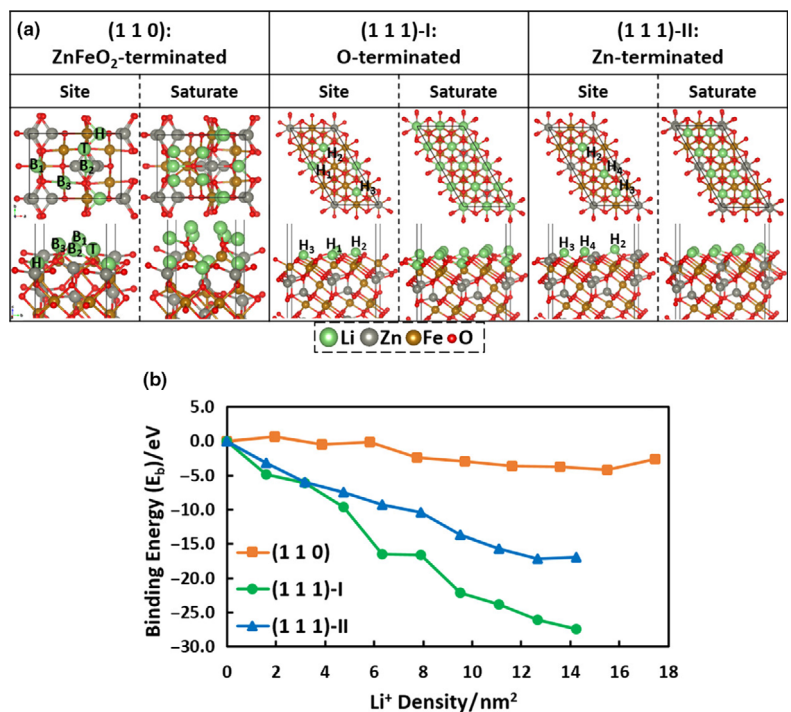


**Figure 18.** a) The optimized structures with Li<sup>+</sup> adsorbed on ZnFe<sub>2</sub>O<sub>4</sub> (110) surface, O-terminated ZnFe<sub>2</sub>O<sub>4</sub> (111) surface, and Zn-terminated ZnFe<sub>2</sub>O<sub>4</sub> (111) surface, above are the corresponding Li<sup>+</sup> saturated structures. b) The plots of binding energies as the function of Li<sup>+</sup> concentration. Reprinted with permission.<sup>[72]</sup> Copyright 2018, American Chemical Society.

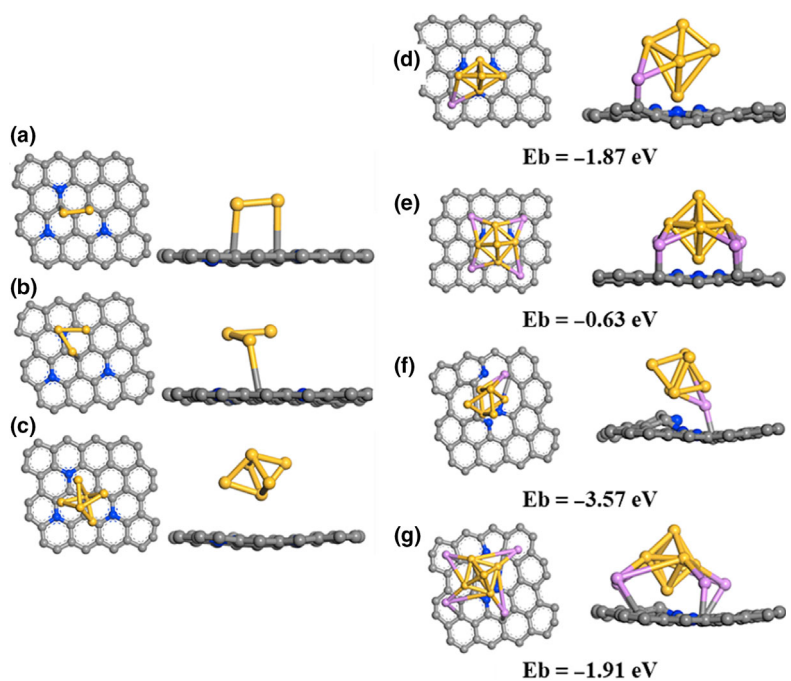


**Figure 19.** DFT optimized structures of a) Si<sub>2</sub>, b) Si<sub>3</sub>, and c) Si<sub>6</sub> clusters adsorbed on graphitic N-doped graphene. Optimized models of single Li and four Li atoms adsorbed on d,e) pyridinic structural NG and f,g) pyrrolic structural NG with Si<sub>6</sub> cluster, respectively. Reprinted with permission.<sup>[73]</sup> Copyright 2018, Elsevier.

higher than those of four Li, no matter on the pyridinic N- or pyrrolic N-doped graphene. In contrast, the pyridinic N-doped graphene is the most effective site for the adsorption of multiple Li ions.

The adsorption kinetics must be taken into consideration when new electrode materials are designed, because it is an important factor for the electrochemical performance of batteries. Li et al.<sup>[38]</sup> have shown that 2D MTe<sub>2</sub> (M = Co, Te, Mn, Ti, Sc) alloys are potential anode materials for SIBs with a detailed analysis of the adsorption kinetics via DFT calculations. Their calculations have shown that the most active adsorption sites for MTe<sub>2</sub> are Te atoms or the centers of hexagonal holes, as shown in **Figure 20**. The adsorption energies of Na ions at different sodiation states were calculated to characterize the adsorption capability of Na ion on various MTe<sub>2</sub>. In Figure 20f, the  $\Delta E$  was defined as:

$$\Delta E = E_{\text{Na}_x\text{MTe}_2} - \left[ \frac{x}{2} E_{\text{Na}_2\text{MTe}_2} + \left(1 - \frac{x}{2}\right) E_{\text{MTe}_2} \right] \quad (12)$$

All of the plots in Figure 20 show the general trend of a decrease at the initial stage and a subsequent increase of adsorption energy. Among these 2D MTe<sub>2</sub>, MnTe<sub>2</sub> can store the largest numbers of Na ions per formula and provide the largest capacity. CoTe<sub>2</sub> is predicted to be unsuitable for SIBs because it can only accommodate 0.25 Na ions per formula, and a distinct distortion of structure occurs after absorbing Na ions.

In summary, DFT calculations can not only assist and support the interpretation of experimental results in battery materials science and technology, but also give predictions and virtual screening of the new battery materials,<sup>[41]</sup> which may significantly shorten the research and development time and reduce the cost.

## 7. Assessment of the DFT Methods for Battery Materials

Although DFT is a powerful tool in computational battery materials science, there are a number of caveats which concern the accuracy of the employed density functionals, and the users should not blindly choose a popular functional for the production runs without validation. The commonly used density functional in battery material science consists of semilocal DFT (LDA, GGA, meta-GGA), GGA+U, and hybrid functional HSE06, and they may suitable for different calculations. The popular semilocal density functional is deficient in dealing with electron correlation effect, and Cococcioni et al.<sup>[74]</sup> have shown that the standard LDA and GGA functionals generate non-negligible errors when electron transfers take place. As for the calculations of electrochemical reaction voltage, the LDA and GGA functionals tend to underestimate the average Li insertion voltages by a fraction of volts, which may be ascribed to the inaccurate treatment of the electronic correlation. The self-interaction of delocalized electron

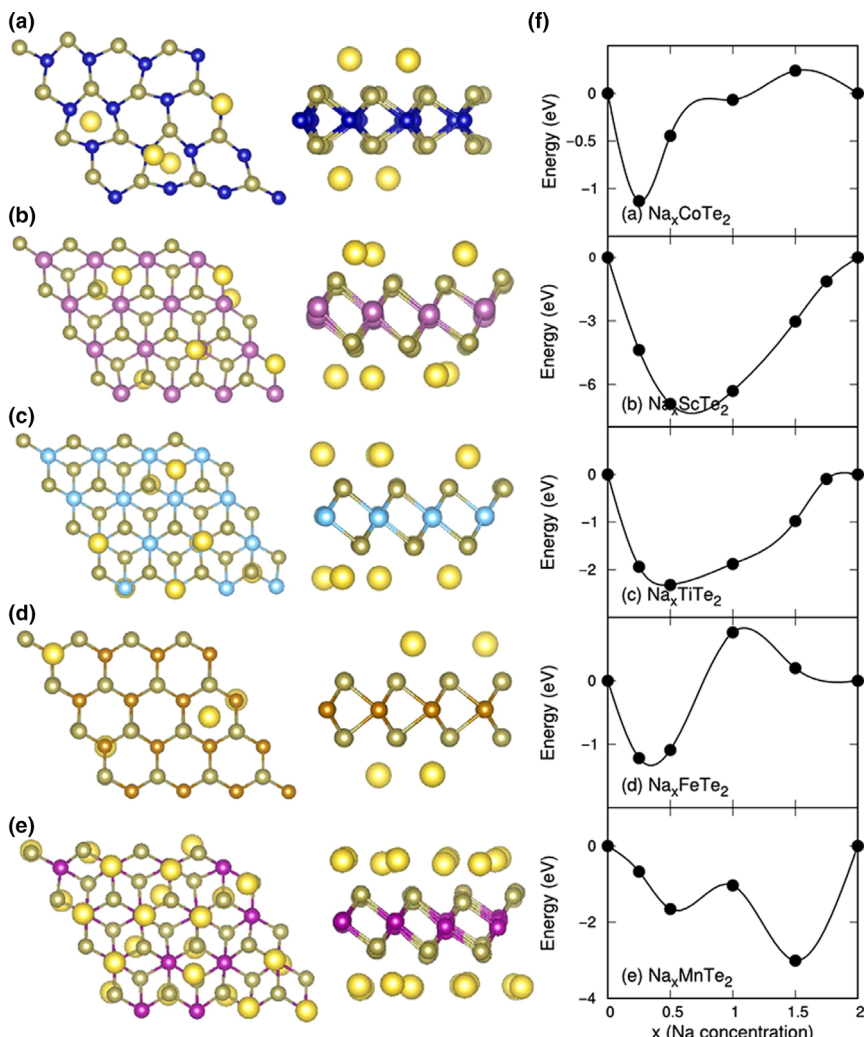


**Figure 20.** The most stable adsorption configurations of Na ions on MT<sub>2</sub>: a) Na<sub>0.25</sub>CoTe<sub>2</sub>, b) Na<sub>0.5</sub>ScTe<sub>2</sub>, c) Na<sub>0.5</sub>TiTe<sub>2</sub>, d) Na<sub>0.25</sub>FeTe<sub>2</sub>, e) Na<sub>1.5</sub>MnTe<sub>2</sub>. f) The plots of  $\Delta E$  of different MT<sub>2</sub> as the function of sodiation state. Reprinted with permission.<sup>[38]</sup> Copyright 2018, Elsevier

of metallic Li is small in LDA/GGA, while it is much larger for localized d-orbital electron of a transition metal (TM) ion. The excessive electron self-interaction causes a lower reaction energy and thus a lower redox voltage, and the reaction energy is underestimated when a delocalized electron changed to be localized. The DFT+U method tackles the problem by decreasing the fractional occupations of Kohn-Sham orbitals. As confirmed by the calculations of lithiation voltage of different TMs structures (Figure 21a), the GGA+U method shows much higher accuracy than GGA.

It is worth noting that the U parameters in the GGA+U method are semi-empirical and system-dependent. In contrast, HSE06 corrects the self-interaction errors by using a portion of the screened HF exchange.<sup>[75]</sup> In 2010, Chevrier et al.<sup>[76]</sup> compared GGA, GGA+U, and HSE06 functionals for the layered LiMO<sub>2</sub>, olivine LiMPO<sub>4</sub>, and spinel-like Li<sub>x</sub>Mn<sub>2</sub>O<sub>4</sub> materials. They have shown that the accuracy of HSE06 is comparable to GGA+U, in terms of formation energy, volume, and Li intercalation potentials. In particular, HSE06 is more accurate than

GGA for the prediction of the formation energy of oxide, while GGA+U is not applicable when it involves TMs because the same U cannot be used to model the metallic states of TMs in their elemental form.

Furthermore, Chevrier et al. found that the electronic structure difference between GGA+U and HSE06 calculations occur in alloys, oxides, and polyanion electrodes.<sup>[76]</sup> For oxides, HSE06 tends to predict more charges on oxygen atoms than GGA+U, and HSE06 gives higher intercalation potentials than GGA+U. However, the situation is different for the polyanion materials, such as LiFePO<sub>4</sub>, and the participation of P weakens the interaction between Fe and O, and the screened HF exchange in HSE06 has less effect on the charge difference, and it gives similar results as GGA+U. Regarding the computational cost of these functionals for solid-state physics, HSE06 computations are much more expensive than GGA+U, especially for the large systems.

As mentioned in Section 4.3, Chakraborty systematically compared the performance of PBE, PBE+U, and the SCAN meta-GGA for the prediction of the properties in three layered cathode materials: LiNiO<sub>2</sub>, LiCoO<sub>2</sub>, and LiMnO<sub>2</sub>.<sup>[61]</sup> Their assessments show that SCAN is better than PBE for the prediction of band gaps and absolute voltages, and SCAN is better than PBE+U for the calculations of DOSS and reaction voltages. The SCAN method is also superior in analyzing electron densities and in operando lattice parameters. The good performance of SCAN could be due to its improved functional form and the enhanced description of medium-range dispersion interactions. The superiority of the SCAN over other semilocal functionals in predicting the structure, electronic states, structural stability, and medium-range vdW interactions have

been reported<sup>[77–79]</sup> recently. However, Isaacs et al.<sup>[80]</sup> pointed out that SCAN gives larger errors for the prediction of the formation energy of weakly bound compounds (such as intermetallic) than the PBE method. In general, SCAN is better than LDA and GGA for the prediction of the properties of battery materials, especially the energy-related calculations. In some cases, it matches the accuracy of the hybrid HSE06 functional, with much lower computational cost.<sup>[78,81]</sup>

He et al.<sup>[82]</sup> recently developed the benchmark LiSAE38 database of 38 atomization energies for lithium polysulfides (Li<sub>2</sub>S<sub>n</sub>, 2 ≤ n ≤ 8) by using AIMD and the recently developed Wuhan–Minnesota Scaling (WMS) method,<sup>[83]</sup> which is a highly accurate wavefunction-based method. The performance of 39 density functionals has been assessed against the LiSAE38 database. Among the tested functionals, the PW6B95, B97-1, B3LYP-D3, TPSS, and DSD-PBEP86 density functionals are the most accurate functionals for the prediction of the absolute atomization energies in lithium polysulfides, whereas the mPW2-PLYP-D, DSD-PBEP86, PW6B95, HSE06, and PBEQIDH functionals are most accurate for the

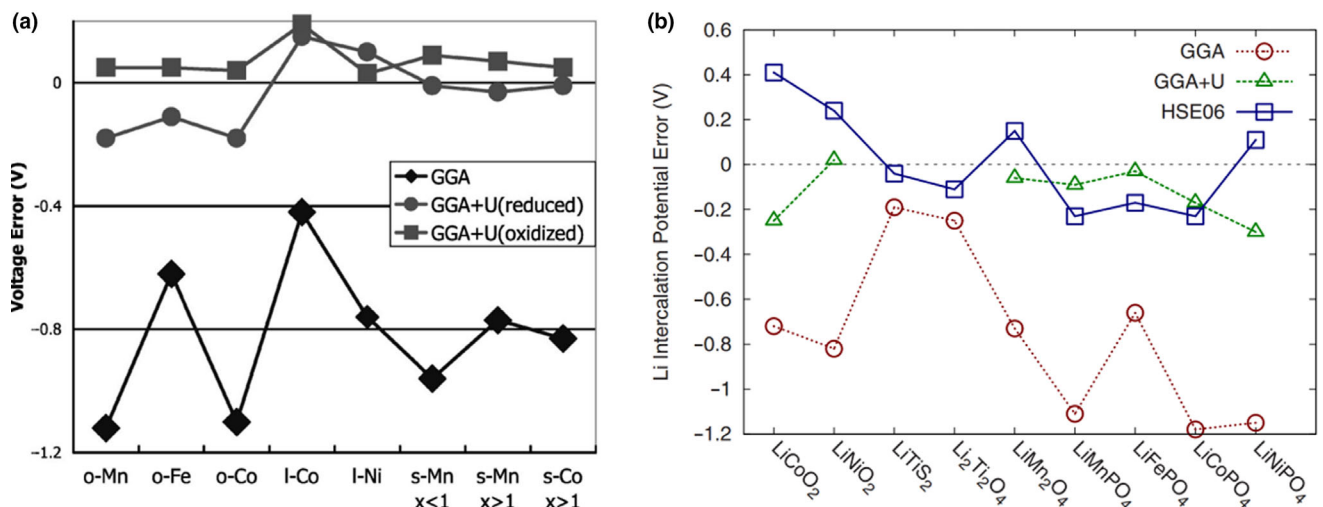


**Figure 21.** a) Comparison of delithiated/lithiated voltage errors of TMs phosphate ( $\text{Li}_x\text{MPO}_4$ ) between GGA and GGA+U with calculated U. (The o, I, and s denote olivine, layered, and spinel, respectively; x represents the lithiation state; the voltage error is obtained by subtracting the experimental voltage from the calculated voltage.) Reprinted with permission.<sup>[74]</sup> Copyright 2004, American Physical Society b) Difference between calculated and experimental Li intercalation potentials for GGA, GGA+U, and HSE06, with respect to different cathode materials. Reprinted with permission.<sup>[76]</sup> Copyright 2010, American Physical Society.

relative energies. The MN15-L and revM06-L methods are the best for the calculations of relative stabilities among the semilocal functionals.

Received: August 9, 2019

Revised: September 24, 2019

Published online: October 15, 2019

## 8. Conclusion

In this review, we summarize the applications of DFT in battery materials science, and several case studies have been discussed in detail to illustrate the theoretical insights that DFT computations can provide for various battery material systems. The DFT mechanistic investigations have contributed significantly to the understanding of the intrinsic properties of battery materials and the electrochemical reaction mechanism, which are essential for developing the next generation of high-performance battery systems. The covered topics include structural stability estimation, reaction voltage and capacity prediction, electronic structures, ionic/molecules transport, and adsorption kinetics in battery systems. Some assessments of DFT for battery systems have been discussed, and our recommendation is to validate the density functionals before the production calculations. We can foresee that the developments of new DFT methods and the designs of novel battery materials will supplement each other in a coordinated manner.

## Acknowledgments

This work was supported by the Excellent Dissertation Cultivation Funds of Wuhan University of Technology (2018-YS-013).

## Conflict of Interest

The authors declare no conflict of interest.

## Keywords

battery, density functional theory, first principle theory, theoretical calculation

- [1] M. M. Aman, K. H. Solangi, M. S. Hossain, A. Badarudin, G. B. Jasmon, H. Mokhlis, A. H. A. Bakar, S. N. Kazi, *Renew. Sust. Energy Rev.* **2015**, *41*, 1190.
- [2] M. R. Islam, S. Mekhilef, R. Saidur, *Renew. Sust. Energy Rev.* **2013**, *21*, 456.
- [3] M. Balat, H. Balat, U. Faiz, *Energy Source Part B* **2009**, *4*, 295.
- [4] S. P. Neill, A. Angeloudis, P. E. Robins, I. Walkington, S. L. Ward, I. Masters, M. J. Lewis, M. Piano, A. Avdis, M. D. Piggott, G. Aggidis, P. Evans, T. A. A. Adcock, A. Zidonis, R. Ahmadian, R. Falconer, *Renew. Energy* **2018**, *127*, 763.
- [5] Q. Li, Y. Liu, S. Guo, H. Zhou, *Nano Today* **2017**, *16*, 46.
- [6] A. Poullikkas, *Renew. Sust. Energy Rev.* **2013**, *27*, 778.
- [7] Y. Miao, P. Hynan, A. von Jouanne, A. Yokochi, *Energies* **2019**, *12*, 1074.
- [8] H. Cha, J. Kim, Y. Lee, J. Cho, M. Park, *Small* **2018**, *14*, e1702989.
- [9] Y. He, B. Matthews, J. Wang, L. Song, X. Wang, G. Wu, *J. Mater. Chem. A* **2018**, *6*, 735.
- [10] X. Zhang, L. Li, E. Fan, Q. Xue, Y. Bian, F. Wu, R. Chen, *Chem. Soc. Rev.* **2018**, *47*, 7239.
- [11] F. Schipper, D. Aurbach, *Russ. J. Electrochem.* **2016**, *52*, 1095.
- [12] K. Kubota, M. Dahbi, T. Hosaka, S. Kumakura, S. Komaba, *Chem. Rec.* **2018**, *18*, 459.
- [13] J. Y. Hwang, S. T. Myung, Y. K. Sun, *Adv. Funct. Mater.* **2018**, *28*, 1802938.
- [14] Q. F. Li, N. J. Bjerrum, *J. Power Sources* **2002**, *110*, 1.
- [15] A. Ponrouch, C. Frontera, F. Bardé, M. R. Palacín, *Nat. Mater.* **2016**, *15*, 169.
- [16] Z. Zhao-Karger, M. Fichtner, *Front. Chem.* **2018**, *6*, 656.
- [17] C. Xu, B. Li, H. Du, F. Kang, *Angew. Chem. Int. Ed.* **2012**, *51*, 933.
- [18] J. Xu, Y. Dou, Z. Wei, J. Ma, Y. Deng, Y. Li, H. Liu, S. Dou, *Adv Sci* **2017**, *4*, p# 1700146.
- [19] R. Chen, R. Luo, Y. Huang, F. Wu, L. Li, *Adv. Sci.* **2016**, *3*, 1600051.
- [20] M. Li, Z. Chen, T. Wu, J. Lu, *Adv. Mater.* **2018**, *30*, e1801190.
- [21] X. P. Han, X. P. Li, J. White, C. Zhong, Y. D. Deng, W. B. Hu, T. Y. Ma, *Adv. Energy Mater.* **2018**, *8*, 1801396.

- [22] S. Q. Zhou, X. Q. Zhang, *Chin. Phys.* **2002**, 11, 1051.
- [23] R. Nityananda, P. Hohenberg, W. Kohn, *Resonance* **2017**, 22, 809.
- [24] G. Ávall, J. Mindemark, D. Brandell, P. Johansson, *Adv. Energy Mater.* **2018**, 8, 1703036.
- [25] Q. Bai, L. Yang, H. Chen, Y. Mo, *Adv. Energy Mater.* **2018**, 8, 1702998.
- [26] X. Chen, T. Hou, K. A. Persson, Q. Zhang, *Mater. Today* **2019**, 22, 142.
- [27] S. Chakraborty, A. Banerjee, T. Watcharatharapong, R. B. Araujo, R. Ahuja, *J. Phys. Condens. Matter* **2018**, 30, 283003.
- [28] K. T. Butler, G. S. Gautam, P. Canepa, *npj Comput. Mater.* **2019**, 5, 19.
- [29] O. Breuer, A. Chakraborty, J. Liu, T. Kravchuk, L. Burstein, J. Grinblat, Y. Kauffman, A. Gladkikh, P. Nayak, M. Tsubery, A. I. Frenkel, M. Talianker, D. T. Major, B. Markovsky, D. Aurbach, *ACS Appl. Mater. Interfaces* **2018**, 10, 29608–29621.
- [30] Y. Bian, W. Zeng, M. He, Y. Ma, Y. Liu, Y. Kong, J. Pan, *J. Colloid Interface Sci.* **2018**, 534, 20.
- [31] M. Nakayama, M. Kaneko, M. Wakihara, *Phys. Chem. Chem. Phys.* **2012**, 14, 13963.
- [32] E. A. Velásquez, D. P. B. Silva, J. B. Falqueto, J. Mejía-López, N. Bocchi, R. del Rio, J. Mazo-Zuluaga, R. C. Rocha-Filho, S. R. Biaggio, *J. Mater. Chem. A* **2018**, 6, 14967.
- [33] L. Wang, L. Deng, Y. Li, X. Ren, H. Mi, L. Sun, P. Zhang, Y. Gao, *Electrochim. Acta* **2018**, 284, 366.
- [34] X. Zhao, Y. Zhao, Z. Liu, Y. Yang, J. Sui, H.-E. Wang, W. Cai, G. Cao, *Chem. Eng. J. (Lausanne)* **2018**, 354, 1164.
- [35] I. H. Lee, J. Cho, K. H. Chae, M. K. Cho, J. Jung, J. Cho, H. J. Lee, H. C. Ham, J. Y. Kim, *Appl. Catal. B* **2018**, 237, 318.
- [36] H. Zhang, X. Liao, Y. Guan, Y. Xiang, M. Li, W. Zhang, X. Zhu, H. Ming, L. Lu, J. Qiu, Y. Huang, G. Cao, Y. Yang, L. Mai, Y. Zhao, H. Zhang, *Nat. Commun.* **2018**, 9, 3729.
- [37] D. Chen, J. H. Wang, T. F. Chou, B. Zhao, M. A. El-Sayed, M. Liu, *J. Am. Chem. Soc.* **2017**, 139, 7071.
- [38] Y.-X. Li, D. B. Putungan, S.-H. Lin, *Phys. Lett. A* **2018**, 382, 2781.
- [39] S. Thomas, E. B. Nam, S. U. Lee, *ACS Appl. Mater. Interfaces* **2018**, 10, 36240.
- [40] A. Sengupta, *Appl. Surf. Sci.* **2018**, 451, 141.
- [41] D. K. Sharma, S. Kumar, A. Laref, S. Auluck, *Computational Condensed Matter* **2018**, 16, e00314.
- [42] H. D. Luong, T. D. Pham, Y. Morikawa, Y. Shibutani, V. A. Dinh, *Phys. Chem. Chem. Phys.* **2018**, 20, 23625.
- [43] T. A. Barnes, L. F. Wan, P. R. C. Kent, D. Prendergast, *Phys. Chem. Chem. Phys.* **2018**, 20, 24877.
- [44] J. Lee, B. Monserrat, I. D. Seymour, Z. Liu, S. E. Dutton, C. P. Grey, *J. Mater. Chem. A* **2018**, 6, 16983.
- [45] X. Qin, M. Shao, P. B. Balbuena, *Electrochim. Acta* **2018**, 284, 485.
- [46] T.-Z. Hou, H.-J. Peng, J.-Q. Huang, Q. Zhang, B. Li, *2D Mater.* **2015**, 2, 014011.
- [47] L. Fang, X. Cao, Z. Cao, *J. Phys.: Condens. Matter* **2019**, 31, 205502.
- [48] B. Mortazavi, A. Dianat, G. Cuniberti, T. Rabczuk, *Electrochim. Acta* **2016**, 213, 865.
- [49] J. Zhu, U. Schwingenschlögl, *2D Mater.* **2016**, 3, 035012.
- [50] G. Liu, X. L. Lei, M. S. Wu, B. Xu, C. Y. Ouyang, *J. Phys. Condens. Matter* **2014**, 26, 355007.
- [51] G. Liu, S. B. Liu, B. Xu, C. Y. Ouyang, H. Y. Song, *J. Appl. Phys.* **2015**, 118, 124303.
- [52] A. Sannayal, Y. Ahn, J. Jang, *Comput. Mater. Sci.* **2019**, 165, 121.
- [53] L. Zhu, Y.-R. Zeng, J. Wen, L. Li, T.-M. Cheng, *Electrochim. Acta* **2018**, 292, 190.
- [54] Y. R. An, X. L. Fan, S. Y. Wang, Z. F. Luo, Y. Hu, Z. H. Xia, *Nanotechnology* **2019**, 30, 085405.
- [55] Y. Ma, *Energy Environ. Mater.* **2018**, 1, 148.
- [56] V. D. V. Anton, J. Bhattacharya, B. A. A. Acc. Chem. Res. **2013**, 46, 1216.
- [57] H. Kim, D. J. Kim, D.-H. Seo, M. S. Yeom, K. Kang, D. K. Kim, Y. Jung, *Chem. Mater.* **2012**, 24, 1205.
- [58] Z. Yao, V. I. Hegde, A. Aspuru-Guzik, C. Wolverton, *Adv. Energy Mater.* **2019**, 9, 1802994.
- [59] J. B. Goodenough, Y. Kim, *Chem. Mater.* **2010**, 22, 587.
- [60] L. Xiong, J. Hu, S. Yu, M. Wu, B. Xu, C. Ouyang, *Phys. Chem. Chem. Phys.* **2019**, 21, 7053.
- [61] A. Chakraborty, M. Dixit, D. Aurbach, D. T. Major, *npj Comput. Mater.* **2018**, 4, 60.
- [62] T. Wu, K. Zhu, C. Qin, K. Huang, *J. Mater. Chem. A* **2019**, 7, 5612.
- [63] Z. Wang, M. Deng, X. Xia, Y. Gao, G. Shao, *Energy. Environ. Mater.* **2018**, 1, 174.
- [64] Z. Wang, X. Niu, J. Xiao, C. Wang, J. Liu, F. Gao, *RSC Adv.* **2013**, 3, 16775.
- [65] J. Meng, Q. He, L. Xu, X. Zhang, F. Liu, X. Wang, Q. Li, X. Xu, G. Zhang, C. Niu, Z. Xiao, Z. Liu, Z. Zhu, Y. Zhao, L. Mai, *Adv. Energy Mater.* **2019**, 9, 1802695.
- [66] X. He, Y. Zhu, A. Epstein, Y. Mo, *npj Comput. Mater.* **2018**, 4, 18.
- [67] C. Jin, W. Zhang, Z. Zhuang, J. Wang, H. Huang, Y. Gan, Y. Xia, C. Liang, J. Zhang, X. Tao, *J. Mater. Chem. A* **2017**, 5, 632.
- [68] Z. Li, S. Zhang, J. Zhang, M. Xu, R. Tatara, K. Dokko, M. Watanabe, *ACS Appl. Mater. Interfaces* **2017**, 9, 38477.
- [69] G. Zhou, E. Paek, G. S. Hwang, A. Manthiram, *Adv. Energy Mater.* **2016**, 6, 1501355.
- [70] C. Li, J. Shi, L. Zhu, Y. Zhao, J. Lu, L. Xu, *Nano Research* **2018**, 11, 4302.
- [71] Q. Zhang, Y. Wang, Z. W. Seh, Z. Fu, R. Zhang, Y. Cui, *Nano Lett.* **2015**, 15, 3780.
- [72] H. Guo, A. C. Marschilok, K. J. Takeuchi, E. S. Takeuchi, P. Liu, *ACS Appl. Mater. Interfaces* **2018**, 10, 35623.
- [73] R. Hu, J. Zhou, *Appl. Surf. Sci.* **2018**, 457, 789.
- [74] F. Zhou, M. Cococcioni, C. A. Marianetti, D. Morgan, G. Ceder, *Phys. Rev. B* **2004**, 70, 235121.
- [75] J. Heyd, J. E. Peralta, G. E. Scuseria, R. L. Martin, *J. Chem. Phys.* **2005**, 123, 174101.
- [76] V. L. Chevrier, S. P. Ong, R. Armiento, M. K. Y. Chan, G. Ceder, *Phys. Rev. B* **2010**, 82, 075122.
- [77] I. G. Buda, C. Lane, B. Barbiellini, A. Ruzsinszky, J. Sun, A. Bansil, *Sci. Rep.* **2017**, 7, 44766.
- [78] G. X. Zhang, A. M. Reilly, A. Tkatchenko, M. Scheffler, *New J. Phys.* **2018**, 20, 060302.
- [79] Y. B. Zhang, D. A. Kitcheva, J. L. Yang, T. N. Chen, S. T. Dacek, R. A. Sarmiento-Perez, M. A. L. Marques, H. W. Peng, G. Ceder, J. P. Perdew, J. W. Sun, *npj Comput. Mater.* **2018**, 4, 9.
- [80] E. B. Isaacs, C. Wolverton, *Phys. Rev. Mater.* **2018**, 2, 063801.
- [81] J. Sun, R. C. Remsing, Y. Zhang, Z. Sun, A. Ruzsinszky, H. Peng, Z. Yang, A. Paul, U. Waghmare, X. Wu, *Nat. Chem.* **2016**, 8, 831.
- [82] Q. He, X. Liao, L. Xia, Z. Li, H. Wang, Y. Zhao, D. G. Truhlar, *J. Phys. Chem. C* **2019**, 123, 20737.
- [83] Y. Zhao, L. Xia, X. Liao, Q. He, M. X. Zhao, D. G. Truhlar, *Phys. Chem. Chem. Phys.* **2018**, 20, 27375.